frontiers in Physics

ORIGINAL RESEARCH
published: 28 January 2019
doi: 10.3389/fphy.2018.00155

Building an Optical Free-Electron Laser in the Traveling-Wave Thomson-Scattering Geometry

Klaus Steiniger[1,2]*, *Daniel Albach*[1], *Michael Bussmann*[1], *Markus Loeser*[1,2], *Richard Pausch*[1,2], *Fabian Röser*[1†], *Ulrich Schramm*[1,2], *Mathias Siebold*[1] and *Alexander Debus*[1]

[1] Institute of Radiation Physics, Helmholtz-Zentrum Dresden-Rossendorf, Dresden, Germany, [2] Institute of Nuclear and Particle Physics, Technische Universität Dresden, Dresden, Germany

We show how optical free-electron lasers and enhanced incoherent Thomson scattering radiation sources can be realized with Traveling-Wave Thomson-Scattering (TWTS) today. Emphasis is put on the realization of optical free-electron lasers (OFELs) with existing state-of-the-art technology for laser systems and electron accelerators. The conceptual design of optical setups for the preparation of laser pulses suitable for TWTS OFELs and enhanced Thomson sources is presented. We further provide expressions to estimate the acceptable alignment tolerances of optical components for TWTS OFEL operation. Examples of TWTS OFELs radiating at 100 nm, 13.5 nm and 1.5 Å as well as an incoherent source producing 30 keV photons highlight the feasibility of the concept and detail the procedure to determine the optical components parameters of a TWTS setup.

Keywords: optical FEL, traveling-wave, Thomson scattering, pulse-front tilt, out-of-focus interaction

OPEN ACCESS

Edited by:
Jerome Faure, UMR7639 Laboratoire d'Optique Appliquée (LOA), France

Reviewed by:
Venu Gopal Achanta, Tata Institute of Fundamental Research, India
Ilia L. Rasskazov, University of Rochester, United States

***Correspondence:**
Klaus Steiniger
k.steiniger@hzdr.de

†***Present Address:***
Fabian Röser, Toptica Photonics AG, Gräfelfing, Germany

Specialty section:
This article was submitted to Optics and Photonics, a section of the journal Frontiers in Physics

Received: *28 September 2018*
Accepted: *17 December 2018*
Published: *28 January 2019*

Citation:
Steiniger K, Albach D, Bussmann M, Loeser M, Pausch R, Röser F, Schramm U, Siebold M and Debus A (2019) Building an Optical Free-Electron Laser in the Traveling-Wave Thomson-Scattering Geometry. Front. Phys. 6:155. doi: 10.3389/fphy.2018.00155

1. INTRODUCTION

With the availability of high-power laser pulses compact ultraviolet to γ-ray radiation sources based on Thomson scattering came into focus of research [1–12]. Most of these Thomson sources produce radiation by scattering high-power laser pulses off relativistic electron bunches in head-on collisions. In the laser field, the oscillatory electron motion is similar to their motion in conventional magnetic undulators employed in synchrotron light sources and free-electron lasers today. Therefore, laser pulses are often referred to as optical undulators in Thomson scattering. While conventional magnetic undulators have undulator periods on the centimeter scale, optical undulators have orders of magnitude smaller periods λ_u since these are determined by the laser wavelength λ_{Laser} which is typically on the micrometer scale. Therefore, Thomson sources can provide hundreds to thousands of undulator periods on submeter interaction distances. Since smaller undulator periods allow for smaller electron energy E_{el} to produce radiation at a target wavelength

$$\lambda \propto \frac{\lambda_u}{E_{el}^2},$$

the footprint of light sources utilizing optical undulators is substantially smaller than those of conventional light sources due to their reduced accelerator length. By additionally utilizing laser wakefield accelerators [13–17] "table-top" all-optical sources were realized with centimeter scale dimensions for electron acceleration and radiation production [18–26].

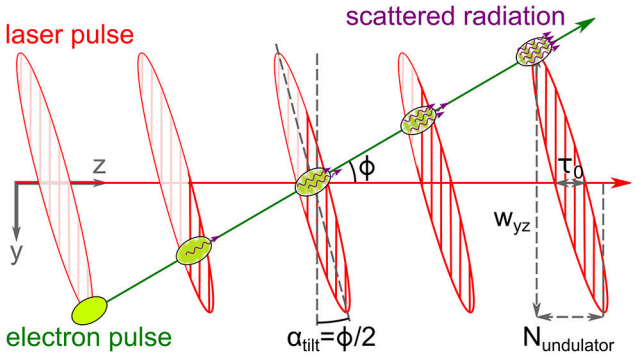

FIGURE 1 | Depicts the Traveling-Wave Thomson-Scattering (TWTS) geometry where electron direction of motion and laser propagation direction enclose the interaction angle ϕ. The laser pulse-front tilt about the angle α_{tilt} ensures continuous overlap of electrons and laser pulse. The combination of side-scattering and laser pulse-front tilt in TWTS allows for the realization of optical undulators where the number of undulator periods $N_{\text{undulator}}$ is not limited by the laser pulse duration τ_0 but instead by the laser pulse width. With current petawatt class laser systems interaction distances long enough for microbunching of the electron pulse and thus coherent amplification of emitted radiation can be realized allowing for compact optical free-electron lasers (OFEL).

Maintaining interaction between electrons and laser pulse over hundreds to thousands of undulator periods can induce microbunching of the electron beam allowing for the realization of optical free-electron lasers (OFELs) [27, 28]. Traveling-Wave Thomson-Scattering (TWTS) [29–31] is able to provide these interaction distances utilizing high-power laser pulses with durations in the femtosecond range. TWTS is scalable from ultraviolet TWTS OFEL realizations to hard X-ray TWTS OFEL realizations.

While in head-on Thomson scattering schemes laser pulse defocusing limits the maximum available interaction distance, TWTS defeats this defocusing limit by exploiting a side-scattering geometry, where laser and electron direction of propagation enclose an interaction angle ϕ as depicted in **Figure 1**. Together with a tilt of the laser pulse-front, the side scattering geometry of TWTS optimizes the overlap between laser pulses and electron bunches during interaction resulting in an increase of monoenergetic scattered photon flux [32] while utilizing the same laser system and electron accelerator as a head-on Thomson geometry ($\phi = 180°$). This enables the realization of TWTS OFELs with existing high-power, short-pulse laser systems and electron accelerator technology [31, 32]. In contrast, proposed OFELs in head-on geometries have extremely challenging requirements on lasers and electron beams [33–35].

Several versions of TWTS OFEL geometries were proposed using either one laser pulse [31, 36, 37] or two laser pulses forming an optical lattice [38–40]. The methods for TWTS pulse preparation presented by Lawler et al. [36], Chang et al. [37, 40] are, however, not suitable for high power laser pulses which are required for TWTS OFEL operation as it is pointed out by Steiniger et al. [31] by analyzing the TWTS OFEL scaling laws for electron bunch and laser pulse requirements. Moreover, the setups of Lawler et al. [36], Chang et al. [37, 40] do not take care of laser pulse dispersion compensation during the electron-laser interaction. Yet, dispersion originates from the laser pulse-front tilt and can inhibit TWTS OFEL operation due to the tight limit on acceptable undulator amplitude variation.

The optical setups presented in this work provide dispersion compensation during the interaction by exploiting the *plane of optimum compression*. Furthermore, they are suitable for high power laser pulses by utilizing only reflective optics and can be realized with currently available technology for laser systems.

We introduce two designs which are both suitable for the realization of incoherent, large interaction angle, hard X-ray TWTS sources and coherent, small interaction angle, ultraviolet to X-ray TWTS OFELs. These designs utilize only a grating pair, planar and cylindrical mirrors. They differ by the ability to focus the laser pulse within the interaction plane, spanned by the electron bunch and laser pulse propagation directions, which may be necessary to reach a target optical undulator strength. In order to design TWTS sources for any target wavelength, we provide extensive scaling formulas to determine optical component parameters and alignment tolerances for both optical setups. Moreover, the latter formulas are generally applicable for the evaluation of acceptable limits on the variation of laser pulse properties to operate a TWTS OFEL. The provided relations are independent of a particular method to generate laser pulses for TWTS and thus can be applied to other possible methods of TWTS OFEL laser pulse generation. Examples accompanying each setup demonstrate their feasibility and exemplify usage of the relations.

2. TRAVELING-WAVE THOMSON-SCATTERING (TWTS)

2.1. TWTS Geometry

Traveling-Wave Thomson Scattering (TWTS) can realize interaction distances much longer than the laser pulse duration and long enough for FEL amplification if the pulse front of the laser is tilted by half the interaction angle $\alpha_{\text{tilt}} = \phi/2$ with respect to the wavefronts. As depicted in **Figure 1**, the pulse-front tilt ensures continuous overlap of electrons and laser pulse allowing to exploit every photon in the laser pulse for scattering. With TWTS the interaction duration is controlled by the laser pulse width. That is, the number of undulator periods $N_{\text{undulator}}$ of a TWTS optical undulator depends on the laser pulse width w_{yz}, which is only limited by the available laser power and size of optics, and the laser wavelength λ_{Laser}

$$N_{\text{undulator}} = \frac{w_{yz}}{\lambda_{\text{Laser}}} \tan \alpha_{\text{tilt}} \,.$$

The TWTS OFEL radiation wavelength λ_{FEL} depends on the interaction angle ϕ. It can be used to control λ_{FEL} independent of electron energy $E_{\text{el}} = \gamma mc^2$ and laser wavelength [41]

$$\lambda_{\text{FEL}} = \frac{\lambda_{\text{Laser}}(1 + a^2/2)}{2\gamma^2(1 - \beta \cos\phi)}\,, \tag{1}$$

where $\beta = v_{el}/c$ is the electron velocity normalized to the speed of light and $a = \lambda_{Laser}\sqrt{I_{Laser}/13.7\,GW}$ is the dimensionless optical undulator strength. It corresponds to the undulator strength parameter K of planar magnetic undulators. The interaction angle ϕ allows to tune λ_{FEL} over orders of magnitude, e.g. from 116 nm at $\phi = 2^\circ$ to 0.04 nm at $\phi = 170^\circ$ for a 40 MeV electron beam and 1 μm laser wavelength.

In TWTS scenarios with large interaction angles, laser pulse dispersion can significantly diminish scattering output. Angular dispersion is naturally present in TWTS through the pulse-front tilt [42]. With angular dispersion (AD) each frequency in the laser pulse propagates in a different direction causing frequency separation in the transverse direction (spatial dispersion) and longitudinal direction (group delay dispersion). Group delay dispersion (GDD) can significantly increase the laser pulse duration which reduces its amplitude and thus photon scattering efficiency. Pulse elongation scales with pulse-front tilt angle α_{tilt}, propagation distance L_{prop} and laser pulse duration τ_0 [42, 43]. Neglecting pulse elongation due to spatial dispersion (SD), the relative change of pulse duration due to GDD is (cf. Equation (47) in **Appendix A**)

$$\frac{\tau'}{\tau_0} = \left[1 + \frac{L_{prop}^2 \lambda_{Laser}^2 \tan^4 \alpha_{tilt}}{\pi^2 (c\tau_0)^4}\right]^{\frac{1}{2}}. \tag{2}$$

Pulse elongation through group delay dispersion can be significant for large scattering angles ($\alpha_{tilt} = \phi/2$) and short laser pulses. On the other hand, it can be negligible for small angles and longer pulses and thus does not affect the photon yield in these setups. Consider as an example two setups, one at $\phi = 160^\circ$, $\tau_0 = 30$ fs and the other at $\phi = 10^\circ$, $\tau_0 = 150$ fs, respectively. For a laser wavelength of $\lambda_{Laser} = 1\,\mu m$ and an interaction distance of $L_{prop} = 25$ cm the short pulse with large tilt elongates to $31000\tau_0$ whereas the long pulse with small tilt elongates to $1.04\tau_0$. That implies one generally needs to take care of laser pulse dispersion, but laser pulse dispersion compensation during the interaction may be omitted when longer laser pulses are applied at small interaction angles.

The two optical setups for TWTS laser pulse preparation presented in sections 3.1 and 3.2 are both capable of fully compensating group delay dispersion during the interaction. Both setups utilize gratings to introduce a pulse-front tilt and provide dispersion compensation during the interaction. They differ by the ability to focus within the interaction plane being spanned by the laser and electron bunch propagation directions. Ideally, dispersion control achieves interaction of the electrons in a bunch with a plane wave laser field. This is important since undulator amplitude and frequency variations must not be too large for OFEL operation. With large variations the FEL instability will not develop. Section 2.3 explains this in more detail and provides limits.

2.2. Pulse-Front Tilt and Dispersion Compensation in TWTS Geometries

TWTS uses high-power laser pulses which require reflective optics for pulse-front tilt generation. That is, setups utilize reflective gratings which introduce angular dispersion. As a consequence, spatial dispersion (SD) and group delay dispersion (GDD) continuously grow in laser pulses for TWTS through frequency separation during propagation and it becomes impossible to create a pulse being free of GDD during the entire interaction. However, it is possible to create a laser pulse being locally free of GDD by exploiting the *plane of optimum compression* being an inherent feature of diffraction at a grating [44]. During propagation the laser pulse crosses this plane part by part where the laser pulse slice currently in the plane of optimum compression is GDD-free while the rest outside the plane is not. As depicted in **Figure 2A**, the plane of optimum compression is oriented obliquely with respect to the laser propagation direction and can be aligned with the electron trajectory.

In TWTS a pair of gratings, similar to a laser pulse compressor, is used to generate and align pulse-front tilt and plane of optimum compression. Both orientations are controlled by the parameters of the grating pair: first and second grating line density, n_1 and n_2 respectively, laser pulse angle of incidence at the first grating $\psi_{in,1}$ and the second grating rotation angle ϵ enclosed by the grating surfaces to allow for non-parallel grating alignment in the setup by rotating the second grating within the horizontal laser plane, see **Figure 2C**.

The position of the plane of optimum compression along the laser propagation path is controlled by a preconditioned group delay dispersion in the incoming pulse. This GDD has the same magnitude but opposite sign as the GDD generated by the passage through the grating pair and subsequent propagation of the tilted pulse to the interaction point. Thus GDD of the incoming pulse can precompensate GDD generated in the setup.

Relations for the orientation of pulse-front tilt α_{tilt} and plane of optimum compression α_{poc} are obtained by expanding the phase $\varphi(\Omega)$ of an angularly dispersed laser pulse with central frequency Ω_0. A frequency Ω within a laser pulse which is subject to angular dispersion, due to diffraction at the first and second grating, propagates in a different direction than the central laser frequency Ω_0, where $\theta(\Omega)$ is the angle enclosed by both propagation directions. Assuming the central frequency propagates along the z-axis, the phase of frequency Ω at a position $\boldsymbol{r} = (y, z)$ can be written as

$$\varphi(\Omega, \boldsymbol{r}) = \boldsymbol{k}(\Omega)\boldsymbol{r} = \frac{\Omega}{c}(z\cos\theta(\Omega) - y\sin\theta(\Omega)).$$

Expanding in powers of $(\Omega - \Omega_0)$ up to second order

$$\varphi(\Omega) \approx \frac{\Omega_0}{c} z + (z - y\tan\alpha_{tilt})\frac{(\Omega - \Omega_0)}{c} + \frac{1}{2}(y\tan\alpha_{poc} - z)\tan^2\alpha_{tilt}\frac{(\Omega - \Omega_0)^2}{\Omega_0 c}, \tag{3}$$

yields relations for α_{tilt} and α_{poc}

$$\tan\alpha_{tilt} = \Omega_0\theta' \qquad \tan\alpha_{poc} = -\frac{2\theta' + \Omega_0\theta''}{\Omega_0\theta'^2}, \tag{4}$$

where $\theta' = \left.\frac{d\theta}{d\Omega}\right|_{\Omega=\Omega_0}$ is the frequency derivative of the deviation angle evaluated at the central frequency. Note that there are

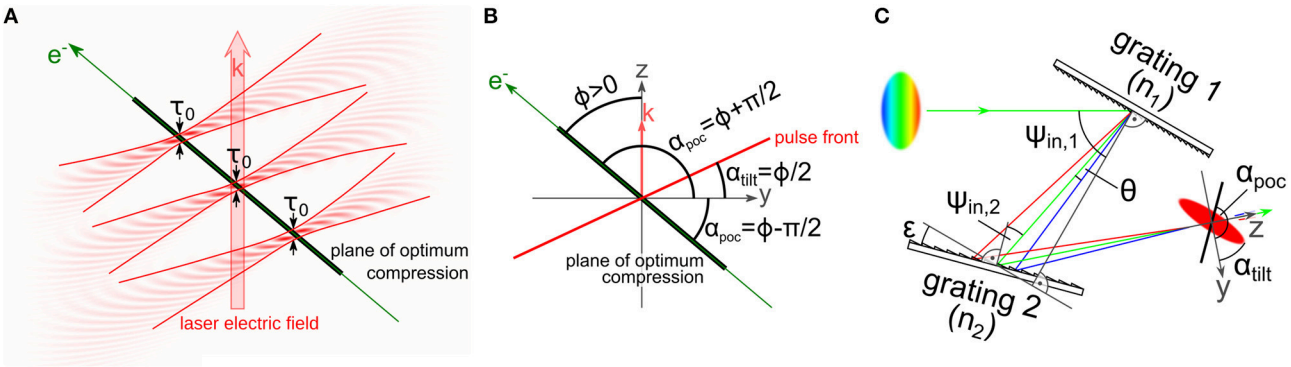

FIGURE 2 | (A) Visualization of the plane of optimum compression. The electric field of a laser pulse traveling upwards is shown three times during Traveling-Wave Thomson-Scattering. Where the laser pulse overlaps with the electron trajectory, it is locally GDD-free manifesting in the shortest possible pulse duration in this region. Away from the electron trajectory, the laser pulse has GDD which increases its duration. **(B)** Shows the angles important when searching for grating setups to form laser pulses for TWTS. As the plane of optimum compression only needs to be aligned with the electron trajectory, there are two possible angles α_{poc} for its orientation. **(C)** Grating pair arrangement for the generation and orientation of pulse-front tilt and plane of optimum compression in TWTS geometries. Parameters controlling pulse-front tilt and plane of optimum compression alignment are first and second grating line density, n_1 and n_2 respectively, laser pulse angle of incidence at the first grating $\psi_{\mathrm{in},1}$ and the second grating rotation angle ϵ measuring its rotation out of parallel alignment to the first grating. The angle θ quantifies the angular deviation of a laser frequency's propagation direction relative to the central laser frequency (green).

always two possible orientations for the plane of optimum compression, but only one possible orientation for the pulse-front tilt.

The phase expansion shows that first order dispersion vanishes along the plane $z = y\tan\alpha_{\mathrm{tilt}}$ defining the pulse-front of the laser. Second order dispersion vanishes along the plane $z = y\tan\alpha_{\mathrm{poc}}$ defining the plane of optimum compression where the pulse duration is transform limited. Expanding the phase to higher orders allows determining the orientation of planes within which these contributions vanish. For example, third order dispersion vanishes along the plane $z = y\tan\alpha_{\mathrm{tod}}$ with $\tan\alpha_{\mathrm{tod}} = (\Omega_0\theta'^3 - 3\theta'' - \Omega_0\theta''')/(\theta'^2 + \Omega_0\theta'\theta'')$. By aligning these planes with the electron trajectory, too, higher order dispersions can be compensated during the interaction, too.

The correct values of pulse-front tilt and plane of optimum compression orientation for TWTS can be identified from **Figure 2B** :

$$\alpha_{\mathrm{poc}} = \phi \pm \pi/2 \qquad \alpha_{\mathrm{tilt}} = \phi/2 \tag{5}$$

Relations (4) and (5) are used to determine parameters of the optical components in the following designs. These relations further express the necessity of a grating pair rather than a single grating since usage of only one grating implies a laser incidence angle of 90° [31].

There is a limitation to this technique as it is only applicable in the case of negligible spatial dispersion during the interaction. This can be estimated by evaluating the pulse elongation due to spatial dispersion during propagation [42, 43]. Neglecting pulse elongation due to GDD, the relative change of pulse duration due to SD is (cf. Equation (47) in **Appendix A**)

$$\frac{\tau}{\tau_0} = \left(1 + \frac{L_{\mathrm{prop}}^2\lambda_{\mathrm{Laser}}^2\tan^2\alpha_{\mathrm{tilt}}}{\pi^2 c^2 \tau_0^2 w_{yz}^2}\right)^{1/2}, \tag{6}$$

where the second term on the right-hand side needs to be small compared to one for spatial dispersion to be negligible. In all practical cases of TWTS this limit is fulfilled, as we aim for long interaction distances requiring pulse width $w_{0,yz}$ on the centimeter scale. The increase in pulse duration from spatial dispersion in the previous long pulse, small interaction angle example is $1.0001\tau_0$. In cases where compensation of spatial dispersion is required, a combination of two varied line-space gratings can be used [30].

2.3. Requirements on Laser Stability for TWTS OFELs

Laser intensity variation, as well as undulator frequency variation, result in a radiation frequency detuning according to the Thomson Formula (1) during interaction. Since the amplified radiation wave advances exactly one wavelength per undulator period with respect to an electron, the detuning must be very small to ensure continuous amplification of the wavelengths within the gain bandwidth around the target OFEL radiation wavelength. Until the TWTS OFEL reaches saturation, the total emission wavelength detuning should be smaller than the FEL gain bandwidth [45], being given by the Pierce parameter ρ [46–48],

$$\frac{\Delta\lambda_{\mathrm{FEL}}}{\lambda_{\mathrm{FEL}}} < 2\rho\,,$$

where for TWTS OFELs [31]

$$\rho = \left[\frac{1}{16\gamma^3}\frac{I_\mathrm{p}}{I_\mathrm{A}}\left(\frac{\lambda_\mathrm{Laser} a f_\mathrm{B}}{2\pi\sigma_\mathrm{el}(1-\beta\cos\phi)}\right)^2\right]^{1/3}$$

with I_p being the electron bunch peak current, σ_el the electron bunch rms cross-sectional radius, $I_\mathrm{A} \approx 17\,\mathrm{kA}$ the Alfvén current, $f_\mathrm{B} = [J_0(\chi) - J_1(\chi)]$ the Bessel function factor with $J_n(\chi)$ being the nth Bessel function of the first kind and $\chi = a^2/(2+a^2)$.

The variation $\Delta\lambda_\mathrm{FEL}/\lambda_\mathrm{FEL}$ due to laser intensity variation ΔI and laser undulator frequency variation $\Delta\tilde{\Omega}$ is found from error propagation of the Thomson formula yielding the limits [31]

$$\frac{\Delta I}{I} = 4\rho\frac{1+a^2/2}{a^2}, \qquad \frac{\Delta\tilde{\Omega}}{\tilde{\Omega}} = 2\rho\,. \tag{7}$$

In order to derive limits on alignment stability in the setups, we will relate variations of setup and optical component parameters to laser amplitude and frequency variations along the electron trajectory and compare these to the above expressions.

3. DESIGN OF OPTICAL SETUPS FOR TWTS

3.1. TWTS Setups Without Focusing Within the Interaction Plane

In TWTS geometries the laser pulse is always focused vertically, i.e., in the plane normal to the interaction plane. Vertical focusing by a cylindrical mirror ensures optimum overlap of laser and electrons in the focus by matching the vertical laser pulse diameter to the electron bunch diameter. Depending on the interaction parameters, e.g., required optical undulator strength and interaction distance, it may be necessary to employ focusing within the interaction plane as well. The design of such setups is presented later.

In the following, we present the design of setups where focusing within the interaction plane can be omitted. Typically, these setups are usable for incoherent hard X-ray Thomson sources and X-ray TWTS OFELs. For example, X-ray TWTS OFELs commonly have gain lengths on the centimeter scale and accordingly require interaction distances on the ten-centimeter scale which are provided by wide laser pulses having widths on the centimeter scale in the interaction plane. The need for pulse widths on the centimeter scale removes the necessity of focusing. Several ten centimeter long interaction distances may be needed for X-ray TWTS OFEL operation since they require thousands of optical undulator periods for a long lasting back reaction of the radiation on the electron bunch which enables coherent radiation amplification through the induced microbunching.

Furthermore, the realization of incoherent yield-enhanced Thomson sources featuring a harmonic-free spectrum with ultra-low bandwidth becomes possible with TWTS offering interaction distances of several ten centimeter. The long interaction distances provided by wide laser pulses allow for large photon yields and enable sub per mille radiation bandwidths since photon yield scales proportionally to the number of undulator periods and bandwidth inversely proportional to it. The sub-relativistic intensity of a wide laser pulse ensures the harmonic-free spectrum. Thus, spectral photon densities of yield-enhanced Thomson sources by TWTS can overtop those of comparable head-on Thomson sources by orders of magnitude [31].

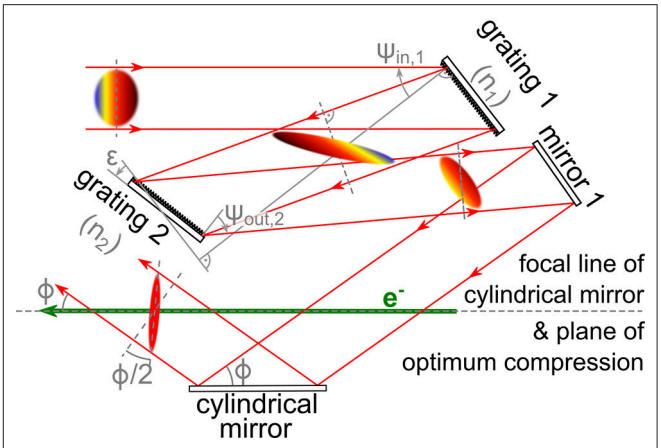

FIGURE 3 | An optical setup for generating TWTS laser pulses with full control over laser pulse dispersion along the electron trajectory. The laser pulse enters the compressor-like grating arrangement from the top left and is incident on the first grating at the angle $\psi_{\mathrm{in},1}$. The two gratings have different line density, n_1 and n_2 respectively, and the second grating is rotated by an angle ϵ with respect to the first grating. The values $\psi_{\mathrm{in},1}, \epsilon, n_1, n_2$ are chosen to realize a pulse-front tilt of half the interaction angle $\alpha_\mathrm{tilt} = \phi/2$ and to align the plane of optimum compression with the electron trajectory $\alpha_\mathrm{poc} = \phi - \pi/2$. The cylindrical mirror provides focusing of the laser pulse in the plane normal to the interaction plane which is spanned by the laser and electron propagation directions. The interaction between electrons and laser takes place after reflection of the laser at the cylindrical mirror. The incoming laser pulse has a non-zero group delay dispersion (GDD) to compensate for GDD arising during propagation to the interaction region after diffraction at the gratings.

The basic design of a setup omitting to focus within the interaction plane is shown in **Figure 3**. An uncompressed laser pulse with residual group delay dispersion (GDD) from a high-power chirped-pulse amplification system enters the grating pair from the top left. The first grating introduces a pulse-front tilt which is corrected and aligned together with the plane of optimum compression according to the Requirements (5) at the second grating. After the second grating, the pulse is redirected at a planar mirror toward the final optical element which is a cylindrical mirror. It provides focusing within the plane normal to the interaction plane, i.e., in the vertical direction, for optimum overlap of laser pulse and electron bunch. The focal line of this cylindrical mirror coincides with the electron bunch trajectory and encloses the angle ϕ with the laser propagation direction. An alternative setup presented later replaces the planar mirror by a cylindrical mirror in order to provide focusing within the interaction plane, i.e., the horizontal direction, too.

Temporal compression of the laser pulse begins after diffraction at the first grating since it introduces angular dispersion to the pulse which is only modified but not removed

by upstream optical elements. Full compression at the interaction point is therefore ensured by attuning group delay dispersion of the incident laser to group delay dispersion acquired during propagation from the first grating to the interaction point.

3.1.1. Laser Pulse Preparation by the Grating Pair

For high diffraction efficiency, high line density gratings with groove spacing $\lesssim 1.25\lambda_{\text{Laser}}$ are used which ensure diffraction only into a single order [49]. These gratings are arranged similarly to the layout of a laser compressor. They face each other but the second grating is rotated out of parallel orientation to the first grating by the angle ϵ. In these compressor-like setups the diffraction angle $\psi_{\text{out},2}$ at the second grating depends on first grating incidence angle $\psi_{\text{in},1}$, line densities of first and second grating, n_1 and n_2 respectively, diffraction order at first and second grating, m_1 and m_2 respectively, as well as second grating rotation angle ϵ.

The orientations of pulse-front tilt and plane of optimum compression after diffraction at the second grating are obtained from the angular deviation $\theta(\Omega)$ between the propagation directions of the central laser frequency Ω_0 and a frequency Ω, as specified by Equation (4), which is given by

$$\begin{aligned} \theta &= \psi_{\text{out},2}(\Omega) - \psi_{\text{out},2}(\Omega_0)\,, \\ \text{where} \qquad \sin\psi_{\text{out},2}(\Omega) &= m_2 n_2 \frac{2\pi c}{\Omega} + \sin(\epsilon - \psi_{\text{out},1}(\Omega))\,, \\ \sin\psi_{\text{out},1}(\Omega) &= m_1 n_1 \frac{2\pi c}{\Omega} + \sin\psi_{\text{in},1}\,. \end{aligned} \tag{8}$$

The respective derivatives of θ can be calculated analytically, yielding

$$\begin{aligned} &\tan\alpha_{\text{tilt},2} = \\ &\frac{\sin(\epsilon - \psi_{\text{out},1}) - \sin\psi_{\text{out},2}}{\cos\psi_{\text{out},2}} - \frac{\cos(\epsilon - \psi_{\text{out},1})}{\cos\psi_{\text{out},2}} \tan\alpha_{\text{tilt},1}\,, \end{aligned} \tag{9}$$

$$\begin{aligned} &\tan\alpha_{\text{poc},2} = -\tan\psi_{\text{out},2} \\ &+ \frac{\left[\sin(\epsilon - \psi_{\text{out},1}) + \cos(\epsilon - \psi_{\text{out},1})\tan\psi_{\text{out},1}\right]}{\cos\psi_{\text{out},2}} \frac{\tan^2\alpha_{\text{tilt},1}}{\tan^2\alpha_{\text{tilt},2}}\,, \end{aligned} \tag{10}$$

for the orientations of pulse-front tilt and plane of optimum compression after the second grating, respectively. The first term in (9) is in its structure equal to the pulse-front tilt after diffraction at a single grating, but the angular dispersion from diffraction at the first grating induces an additional pulse-front rotation expressed by the second term. Similarly, the first term in the expression for the plane of optimum compression orientation (10) is equal to the value after diffraction at a single grating and the second term modifies this value due to angular dispersion from diffraction at the first grating.

Examples demonstrating the achievable range in pulse-front tilt and plane of optimum compression orientation angles for several grating combinations are presented in **Figure 4**. Graphs in the left column refer to a setup where the first grating has a line density of 800 l/mm and the incidence angle at this grating is 18°. Graphs in the right column refer to a setup where the first grating has a line density of 1600 l/mm and the incidence angle at this grating is 61°. In both setups the first grating incidence angle is chosen close to the grating's Littrow angle for high diffraction efficiency. In each column, the first plot shows the scaling of pulse front tilt with second grating rotation angle for three different second gratings which differ in line density. These are 1000, 1200, and 1400 l/mm. The second plot in each column shows the corresponding scaling of plane of optimum compression orientation. These scalings show that in both cases, lowest and highest line density at the first grating, the difference in line density between the two gratings mainly allows controlling the pulse-front tilt, while the second grating rotation angle ϵ mainly controls the plane of optimum compression orientation.

As in TWTS both α_{tilt} and α_{poc} depend on the interaction angle ϕ, their scalings must be seen in combination. According to **Figure 2B** and Equation (5) the condition for a well-designed TWTS geometry can be expressed as

$$\alpha_{\text{poc}} - 2\alpha_{\text{tilt}} = \pm\frac{\pi}{2}\,. \tag{11}$$

The last plot in each column shows which values of second grating rotation angle ϵ fulfill this condition for the different gratings setups. In the case of a higher line density at the first grating (right column) more parameter sets for TWTS are found resulting from larger control over plane of optimum compression orientation compared to the case with a lower line density at the first grating (left column).

On the other hand, larger control comes on the cost of more sensitive alignment since variations have a larger impact on the orientations of plane of optimum compression and pulse-front tilt. Later, we derive limits for alignment tolerances in TWTS OFEL setups, which connect misalignment to intensity and frequency variations during the interaction, since too large variations can inhibit lasing of an FEL.

3.1.2. Determining Grating Parameters

In order to determine the grating parameters for a target interaction geometry with preset interaction angle ϕ, the analytical solutions for pulse-front tilt and plane of optimum compression, Equations (9) and (10) respectively, can be utilized. In a first iteration step, some values for the first grating incidence angle $\psi_{\text{in},1}$ and line density n_1 are assumed allowing to recast the analytic solutions into defining equations for second grating line density n_2 and incidence angle $\psi_{\text{in},2} = \epsilon - \psi_{\text{out},1}$. These defining equations are obtained by first deriving an expression for the sine of the second grating incidence angle $s_{\text{i}} = s_{\text{i}}(s_{\text{o}}, \psi_{\text{in},1}, n_1, \phi) = \sin(\epsilon - \psi_{\text{out},1})$ by rearranging (9) into an equation for $\sin\psi_{\text{in},2} - \cos\psi_{\text{in},2}\tan\alpha_{\text{tilt},1}$, multiplying it by $\tan\psi_{\text{out},1}$ and adding to it the equation obtained by rearranging (10) for $\sin\psi_{\text{in},2} + \cos\psi_{\text{in},2}\tan\psi_{\text{out},1}$ which is multiplied by $\tan\alpha_{\text{tilt},1}$. The equation for s_{i} depends on the sine of the second grating diffraction angle, $s_{\text{o}} = s_{\text{o}}(s_{\text{i}}, \psi_{\text{in},1}, n_1, \phi) = \sin\psi_{\text{out},2}$, for which an equation is found in a similar manner to s_{i},

$$s_{\text{i}} = \frac{\frac{\tan^2(\phi/2)}{\tan\alpha_{\text{tilt},1}}\left(s_{\text{o}} - \sqrt{1-s_{\text{o}}^2}\cot\phi\right) + \left(s_{\text{o}} + \sqrt{1-s_{\text{o}}^2}\tan(\phi/2)\right)\tan\psi_{\text{out},1}}{\tan\alpha_{\text{tilt},1} + \tan\psi_{\text{out},1}}$$

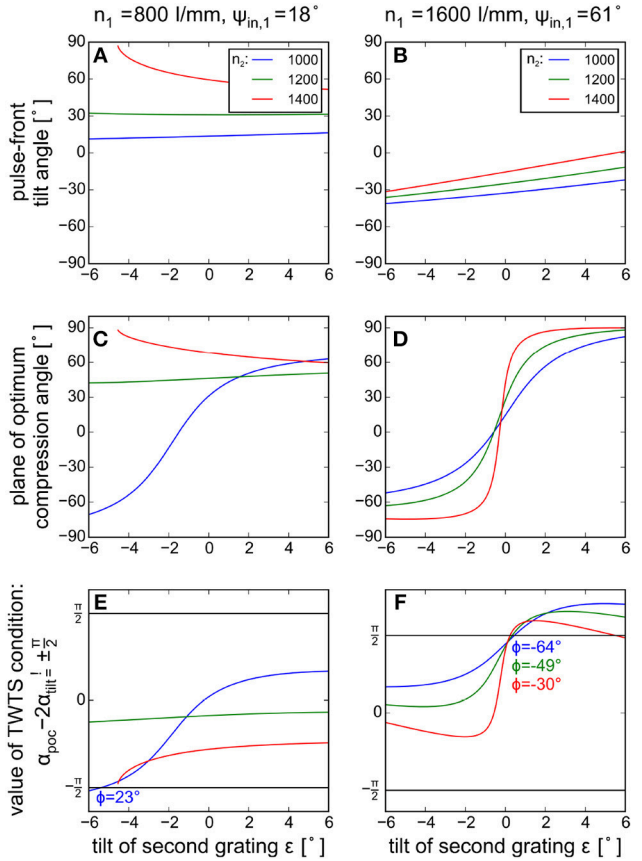

FIGURE 4 | Scaling of pulse-front tilt angle α_{tilt} **(A,B)**, plane of optimum compression angle α_{poc} **(C,D)** and Condition (11) for correct alignment of α_{tilt} and α_{poc} for TWTS in dependence of the rotation angle ϵ of the second grating **(E,F)**, compare **Figure 3**. In scalings **(A,C,E)** the line density n_1 of the first grating is smaller than that of the second grating n_2 while in **(B,D,F)** $n_1 > n_2$. In all scalings diffraction is into −1st order at both gratings. For setups fulfilling the TWTS condition, the interaction angle is given in **(E,F)**. The first grating incidence angles $\psi_{\text{in},1}$ are chosen close to the respective Littrow angles for optimum diffraction efficiency.

$$s_{\text{o}} = \frac{\frac{\tan^2\alpha_{\text{tilt},1}}{\tan(\phi/2)}\left(s_{\text{i}} + \sqrt{1-s_{\text{i}}^2}\tan\psi_{\text{out},1}\right) + \left(s_{\text{i}} - \sqrt{1-s_{\text{i}}^2}\tan\alpha_{\text{tilt},1}\right)\cot\phi}{\tan(\phi/2)+\cot\phi}, \tag{12}$$

using the Conditions (5) and where the diffraction angle $\psi_{\text{out},1}$ and the pulse-front tilt angle $\alpha_{\text{tilt},1}$ after the first grating are given by

$$\sin\psi_{\text{out},1}(\Omega) = m_1 n_1 \frac{2\pi c}{\Omega} + \sin\psi_{\text{in},1} \tag{13}$$

$$\tan\alpha_{\text{tilt},1} = \frac{\sin\psi_{\text{in},1} - \sin\psi_{\text{out},1}}{\cos\psi_{\text{out},1}}. \tag{14}$$

From Equation (12) the second grating parameters $(\psi_{\text{in},2}, n_2)$ are determined from the first grating parameters $(\psi_{\text{in},1}, n_1)$ and the interaction angle ϕ by solving the implicit equation for s_{i} which is obtained by inserting the expression for s_{o} into the expression for s_{i}. The solution $s_{\text{i,sol}}$ is related to the second grating rotation angle ϵ by

$$\epsilon = \psi_{\text{in},2} - \psi_{\text{out},1} = \arcsin s_{\text{i,sol}} - \psi_{\text{out},1}. \tag{15}$$

The second grating line density is determined from this solution, too, and from the corresponding solution $s_{\text{o,sol}} = s_{\text{o}}(s_{\text{i,sol}}, \psi_{\text{in},1}, n_1, \phi)$ by

$$n_2 = \frac{s_{\text{o,sol}} - s_{\text{i,sol}}}{\lambda_{\text{Laser}} m_2}. \tag{16}$$

The order of diffraction at the second grating m_2 is determined by the sign of $s_{\text{o,sol}} - s_{\text{i,sol}}$ in this expression through the requirement of a positive n_2.

This procedure of second grating parameter determination may be repeated for a different set of first grating parameters $(\psi_{\text{in},1}, n_1)$ in order to optimize the second grating parameters for a target interaction geometry at interaction angle ϕ. In this way, the parameters of both gratings can be optimized for e.g., diffraction efficiency, standard line densities or a target laser pulse width after passing the grating pair.

The fact that there is a range of grating parameters resulting in the same orientation of pulse-front tilt and plane of optimum compression has an important implication on the variability of a TWTS light source with respect to the radiation wavelength created. This variability implies that a range of TWTS sources operating at different interaction angles can be built with a single grating pair combination, where only alignment angles change. **Figure 5** illustrates that a grating pair with first grating line density $n_1 = 800\,\text{l/mm}$ and second grating line density $n_2 = 1000\,\text{l/mm}$ can be used to operate TWTS sources at interaction angles from 22° to 42° while ensuring diffraction at the gratings only into −1st order.

3.1.3. Limits on Variations in Laser Pulse Properties and Optical Setup Parameters for TWTS OFEL Realization

One important aspect in building an FEL is providing an undulator field as close to a plane wave as possible, cf. section 2.3. Variations in laser intensity and frequency along the electron trajectory translate to distortions of the optical undulator field. These variations can originate from potentially present higher-order dispersions as well as misalignment of pulse-front tilt and plane of optimum compression. These misalignments can be caused by misalignments of gratings $(\Delta\psi_{\text{in},1}, \Delta\epsilon)$ or laser and electron beam pointing $(\Delta\phi)$.

Estimates for intensity and frequency variations during the interaction due to variations in pulse-front tilt and plane of optimum compression are obtained from an expression for the electric field of a Gaussian laser pulse with dispersions. This expression is obtained by an inverse Fourier transform of an electric field with a phase term equal to Equation (3)

$$E(z,y,t) = \frac{1}{2\pi}\int \mathrm{d}\Omega\, \mathrm{e}^{i\Omega t}\hat{E}_0 \mathrm{e}^{-(\Omega-\Omega_0)^2\tau_0^2/4}\mathrm{e}^{-i\varphi(\Omega)}$$

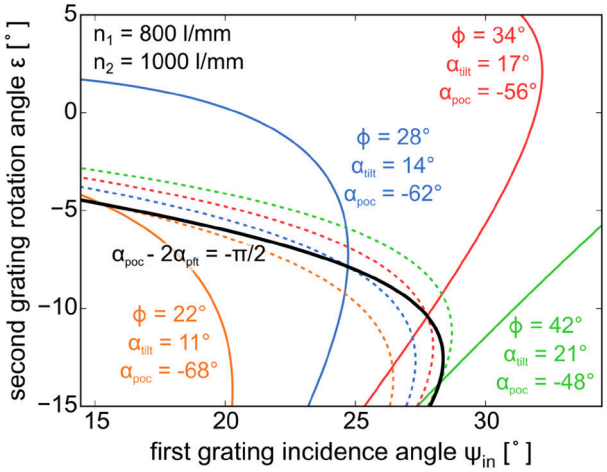

FIGURE 5 | Possible combinations of first grating incidence angle $\psi_{\text{in},1}$ and second grating rotation angle ϵ yielding a well-designed TWTS setup with correct orientation of pulse-front tilt and plane of optimum compression for a single grating pair (black line). The first and second grating line densities are $n_1 = 800\,\text{l/mm}$ and $n_2 = 1000\,\text{l/mm}$, respectively. The laser wavelength is $\lambda_{\text{Laser}} = 1.035\,\mu\text{m}$. Colored solid lines connect combinations $(\psi_{\text{in},1}, \epsilon)$ which keep a pulse-front tilt orientation constant. Colored dashed lines connect combinations $(\psi_{\text{in},1}, \epsilon)$ which keep a plane of optimum compression orientation constant. Pulse-front tilt and plane of optimum compression orientation for curves of equal color are chosen as required for a well-designed TWTS setup at some interaction angle ϕ. A pair of first grating incidence angle and second grating rotation angle belonging to a well-designed TWTS setup is given by an intersection point of two equal colored lines, i.e., Condition (11) is fulfilled at the intersection. All graphs together demonstrate a variability in interaction angle from 22° to 42° for this particular grating pair. The radiation wavelength of a TWTS light source operated by this grating pair can be reduced by a factor of 3.5 by changing the interaction angle from 22° to 42° without replacing optical components or changing the electron energy.

$$= \frac{E_0}{[1+D^2]^{1/4}} \mathrm{e}^{-L^2/(1+D^2)} \mathrm{e}^{i\frac{\Omega_0}{c}(ct-z)} \mathrm{e}^{-i\frac{1}{2}\arctan D} \mathrm{e}^{iDL^2/(1+D^2)}. \tag{17}$$

Therein

$$L(y,z) = \frac{ct - z + y\tan\alpha_{\text{tilt}}}{c\tau_0} \quad \text{and}$$
$$D(y,z) = \frac{2(y\tan\alpha_{\text{poc}} - z)\tan^2\alpha_{\text{tilt}}}{\Omega_0 c\tau_0^2} \tag{18}$$

quantify the distance of some point (y, z) to the laser pulse-front along its propagation direction z and to the plane of optimum compression, respectively. When evaluating the field along the electron trajectory $(y_{\text{el}}(t), z_{\text{el}}(t))$, $D(y_{\text{el}}, z_{\text{el}})$ becomes a measure of laser dispersion and $L(y_{\text{el}}, z_{\text{el}})$ of electron and laser overlap. The laser field will resemble a plane wave ($D = \text{const}$, $L = \text{const}$), if pulse-front tilt and plane of optimum compression are optimally aligned. That is, they need to be oriented according to (5) for electrons traveling along the trajectory

$$z_{\text{el}} = (ct+u)\cos\phi + v\sin\phi \quad y_{\text{el}} = -(ct+u)\sin\phi + v\cos\phi, \tag{19}$$

where $u = v = 0$ corresponds to the electron bunch center trajectory with u and v representing a longitudinal and transverse offset of a single electron from the bunch center, respectively.

Ideally, the laser field resembles a plane wave over the whole electron bunch, while in reality the laser intensity, as well as undulator frequency, can vary within the bunch or during the interaction due to non-optimum overlap or dispersion. These variations will occur if electrons are located far from the bunch center or optics are not ideally aligned, respectively. Therefore, on the one hand, the laser pulse duration must be large enough in order to provide good overlap. On the other hand, alignment errors must be kept within the tolerance limits to prevent loss of overlap and optical undulator frequency detuning to achieve OFEL operation.

According to standard rules for maximum error estimation, a variation of laser intensity I and optical undulator frequency $\tilde{\Omega} = \Omega_0/(1-\cos\phi)$ is related to variations ΔD, $\Delta\dot{D}$ and ΔL of the dispersion term D, its temporal derivative $\dot{D}$ and the overlap term L, respectively, by

$$\left|\frac{\Delta I}{I}\right| = \frac{\Delta D^2}{2} + 2\Delta L^2, \tag{20}$$
$$\left|\frac{\Delta\tilde{\Omega}}{\tilde{\Omega}}\right| = \frac{\lambda_{\text{Laser}}}{4\pi c(1-\cos\phi)}\Delta\dot{D} \tag{21}$$

which are limited by Relations (7).

For optimum alignment, there is no frequency variation within the electron bunch and during the interaction, i.e., $\Delta\tilde{\Omega} = 0$ for all (u, v), but there is an intensity variation within the bunch. Relation (20) together with its Limit (7) provide an approximation for the electron bunch duration and width, i.e., maximum values of u and v respectively, that result in acceptable intensity variation within the electron bunch for a given laser pulse duration. In this case of optimum alignment, the dispersion and overlap terms for electrons at the rim of the bunch ($u \approx c\tau_{\text{el}}, v \approx \sigma_{\text{el}}$) become

$$\Delta D = \frac{\lambda_{\text{Laser}}\tan^2(\phi/2)}{\pi(c\tau_0)^2}\sigma_{\text{el}} \tag{22}$$
$$\Delta L = \frac{c\tau_{\text{el}} + \sigma_{\text{el}}\tan(\phi/2)}{c\tau_0} \tag{23}$$
$$\Delta\left[\frac{\mathrm{d}D}{\mathrm{d}t}\right] = 0 \tag{24}$$

which is obtained by inserting the electron trajectory as well as Equation (5) into the expressions for D and L.

Alignment errors in pulse-front tilt $\Delta\tan\alpha_{\text{tilt}}$, plane of optimum compression $\Delta\tan\alpha_{\text{poc}}$ and interaction angle $\Delta\phi$ result in dispersion, reduced overlap and optical undulator frequency drift until the end of interaction ($t_{\text{end}} = L_{\text{int}}/2c$). Accordingly, the dispersion term, its time derivative and the overlap term evolve to

$$\Delta D = \frac{\lambda_{\text{Laser}}}{\pi c^2\tau_0^2}\left\{\left[-\frac{L_{\text{int}}}{2}\sin\phi + \sigma_{\text{el}}\cos\phi\right]\tan^2(\phi/2)\Delta\tan\alpha_{\text{poc}} - 2\sigma_{\text{el}}\frac{\tan(\phi/2)}{\sin\phi}\Delta\tan\alpha_{\text{tilt}} + \tan^2(\phi/2)\frac{L_{\text{int}}}{2\sin\phi}\Delta\phi\right\}$$

$$\Delta L = \frac{1}{c\tau_0}\left[\left(\frac{L_{\mathrm{int}}}{2}\sin\phi - \sigma_{\mathrm{el}}\cos\phi\right)\Delta\tan\alpha_{\mathrm{tilt}} - \left(\frac{L_{\mathrm{int}}}{2}\tan(\phi/2) - \sigma_{\mathrm{el}}\right)\Delta\phi\right] \quad (25)$$

$$\Delta\left[\frac{\mathrm{d}D}{\mathrm{d}t}\right] = \frac{\lambda_{\mathrm{Laser}}\tan^2(\phi/2)}{\pi c\tau_0^2}\left(\frac{\Delta\phi}{\sin\phi} - \sin\phi\,\Delta\tan\alpha_{\mathrm{poc}}\right)$$

by then. These expressions are again an estimate for the maximum variation obtained by error propagation.

In order to find upper limits for the grating alignment tolerances of first grating incidence angle $\Delta\psi_{\mathrm{in},1}$ and second grating rotation angle $\Delta\epsilon$, it is practical to begin by slightly varying the parameters of a well-designed TWTS setup and recording the resulting changes in pulse-front tilt, as well as plane of optimum compression, via (4). These are used to evaluate variations in laser intensity (20) and laser undulator frequency (21) which are calculated via (25) and compared to the allowed Limits (7).

3.2. TWTS Setups Providing Focusing Within the Interaction Plane

TWTS OFEL operation may require laser pulse focusing within the interaction plane, spanned by the electron and laser propagation direction, in order to achieve optical undulator strengths a on the order of unity. Focusing spatially dispersed laser pulses with a parabolic mirror is a convenient method to simultaneously generate the pulse-front tilt while keeping the intensity on optics below their damage threshold [50]. Laser pulses for TWTS OFELs, which require pulse widths on the centimeter scale at the interaction point, have Rayleigh length on the one hundred meter scale. This will result in focal distances of many hundred meters for petawatt-class lasers, if the interaction point had to coincide with the focus.

However, the propagation distance can be significantly reduced by an out-of-focus interaction geometry as depicted in **Figure 6**. In the out-of-focus geometry, the interaction point of electron bunch and laser pulse is not in the focus but rather outside the focus between the focal point and the off-axis cylindrical mirror providing focusing within the interaction plane. Since the interaction takes place before the focus where the laser pulse width is still large, this geometry allows to strongly focus the laser pulse to a focal width smaller than required to operate the TWTS OFEL. Thus, a significant reduction of the Rayleigh length and focal distance can be achieved.

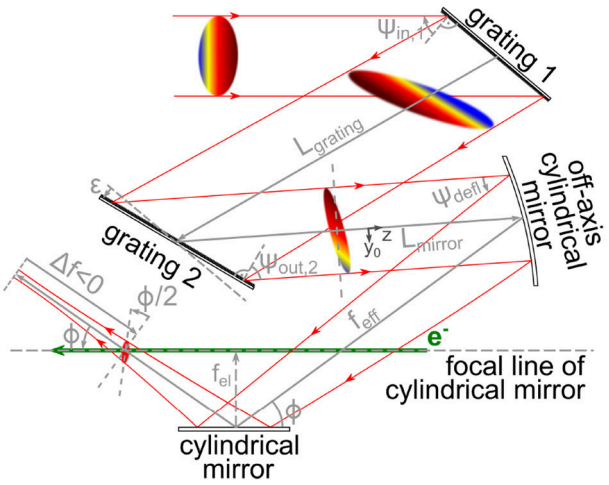

FIGURE 6 | An optical setup to generate focused TWTS laser pulses where pulse-front tilt arises from spatial dispersion in the pulse before focusing. A chirped laser pulse enters from the top left a two grating setup under the angle $\psi_{\mathrm{in},1}$ in order to transversely separate its frequencies by angular dispersion and propagation about the distance L_{grating}. Rotating the second grating by an angle ϵ out of parallel orientation to the second grating, removes most of the angular dispersion, but leaves a small residual pulse-front tilt. The laser pulse exits the two grating setup under the angle $\psi_{\mathrm{out},2}$. Focusing the laser pulse in both transverse dimensions is achieved in two steps. First, focusing in the horizontal direction, i.e., in the interaction plane spanned by the electron trajectory and the laser propagation direction, is provided by an off-axis cylindrical mirror of effective focal length f_{eff}. It turns spatial dispersion into angular dispersion thereby generating the required pulse-front tilt $\phi/2$ of half the interaction angle ϕ. Second, optimum overlap of laser and electrons is ensured by the second cylindrical mirror focusing in the vertical direction, i.e. normal to the interaction plane. Interaction takes place a distance Δf before the actual focus of the off-axis cylindrical mirror. Vanishing spatial dispersion at the interaction point, and not at the actual focus of the off-axis cylindrical mirror, is ensured by the residual pulse-front tilt after the second grating.

3.2.1. Pulse-Front Tilt Generation at an Off-Axis Cylindrical Mirror

In order to simultaneously focus a laser and tilt its pulse front, the pulse is spatially dispersed first and then focused by an off-axis cylindrical mirror. Focusing a spatially dispersed laser pulse by an off-axis cylindrical mirror introduces angular dispersion which translates to a pulse-front tilt, cf. Equation (4). Subsequently, focusing reduces spatial dispersion and ensures spatial overlap of the frequencies while the pulse propagates to the interaction point. **Figure 7** depicts this principle and shows that the position where the frequencies completely overlap, i.e., spatial dispersion vanishes, can be controlled by an initial angular dispersion of the pulse introduced prior to deflection at the off-axis cylindrical mirror.

In this out-of-focus interaction geometry, initial angular and spatial dispersion are provided by a grating pair just as it is utilized in the setup without focusing. Accordingly, the analytical results for pulse-front tilt and plane of optimum compression orientation after diffraction at the second grating, Equations (9) and (10) respectively, are reused for this setup providing focusing to obtain analytical relations for their orientation at the interaction point.

3.2.2. Orientation of Pulse-Front Tilt and Plane of Compression

After deflection at the focusing mirror, a frequency's propagation angle $\theta(\Omega)$ relative to the central laser frequency's propagation direction is given by the angle $\theta_{\mathrm{in}}(\Omega)$, which is enclosed by both propagation directions before deflection at the mirror, as well as the frequency's incidence point on the mirror surface $y_{\mathrm{in}}(\Omega)$ and the deflection angle of the central frequency $\psi_{\mathrm{defl}}(\Omega_0)$

$$\theta(\Omega) = \psi_{\mathrm{defl}}(\Omega) - \theta_{\mathrm{in}}(\Omega) - \psi_{\mathrm{defl}}(\Omega_0)\,. \quad (26)$$

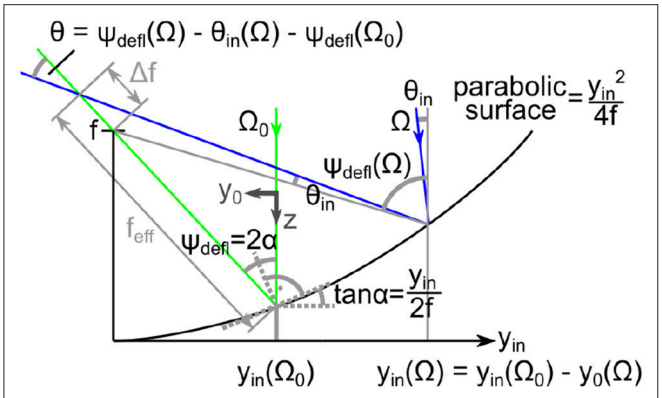

FIGURE 7 | Coordinate system used for the calculation of pulse-front tilt from focusing a spatially dispersed laser pulse at an off-axis cylindrical mirror with parent focal distance f. Spatial dispersion of the incident laser pulse results in an individual incidence position $y_{\text{in}}(\Omega)$ of each frequency Ω on the mirror surface. Each frequency is therefor deflected by a different angle $\psi_{\text{defl}}(\Omega)$ determining the angular deviation $\theta(\Omega) = \psi_{\text{defl}}(\Omega) - \theta_{\text{in}}(\Omega) - \psi_{\text{defl}}(\Omega_0)$. The individual incidence angle of each frequency θ_{in} determines the distance Δf from the actual focus of the off-axis cylindrical mirror after which spatial dispersion vanishes. For the TWTS OFEL out-of-focus setup, θ_{in} is controlled by the grating setup $\theta_{\text{in}}(\Omega) = \psi_{\text{out},2}(\Omega) - \psi_{\text{out},2}(\Omega_0)$.

The deflection angle of frequency Ω is

$$\psi_{\text{defl}}(\Omega) = 2\arctan(y_{\text{in}}(\Omega)/2f)\,,$$

and its incidence position on the mirror surface is

$$y_{\text{in}}(\Omega) = y_{\text{in}}(\Omega_0) - y_0(\Omega)\,,$$

where y_0 is the distance of a frequency's spatial distribution center from the laser pulse axis. Deflection angle and incidence position both depend on this distance which quantifies spatial dispersion of the pulse generated during propagation from first to second grating and from second grating to off-axis cylindrical mirror

$$y_0(\Omega) = L_{\text{grating}}\tan\theta_1(\Omega) - L_{\text{mirror}}\tan\theta_2(\Omega)\,,$$

with $\theta_1(\Omega)$ and $\theta_2(\Omega)$ being the angles enclosed by the propagation directions of frequency Ω and the central laser frequency after diffraction at the first and second grating, respectively. Further, L_{grating} is the distance between the gratings and L_{mirror} the distance from the second grating to the off-axis cylindrical mirror. The deviation in propagation direction before deflection at the focusing mirror $\theta_{\text{in}}(\Omega)$ is related to angular dispersion from the grating pair

$$\theta_{\text{in}}(\Omega) = \psi_{\text{out},2}(\Omega) - \psi_{\text{out},2}(\Omega_0) = \theta_2(\Omega)\,,$$

where $\psi_{\text{out},2}$ is the diffraction angle at the second grating, as before in the setup without focusing. In the relation for the deflection angle, the quantity f is the parent focal distance of the off-axis cylindrical mirror. Its effective focal distance, which is the distance traveled by the central laser frequency to the focal line, is

$$f_{\text{eff}} = \frac{f}{\cos^2(\psi_{\text{defl}}(\Omega_0)/2)}\,.$$

From the expression for the frequency specific propagation angle 26, the orientation of pulse-front tilt and plane of optimum compression at the interaction point can be derived analytically, c.f. Equation (4). These are

$$\begin{aligned}
\tan\alpha_{\text{tilt}} &= \frac{\cos\psi_{\text{out},2}}{\cos\psi_{\text{in},2}}\frac{L_{\text{grating}}}{f_{\text{eff}}}\tan\alpha_{\text{tilt},1} - \left(\frac{L_{\text{mirror}}}{f_{\text{eff}}} - 1\right)\tan\alpha_{\text{tilt},2} \\
\tan\alpha_{\text{poc}} &= \frac{\cos\psi_{\text{out},2}}{\cos\psi_{\text{in},2}}\frac{L_{\text{grating}}}{f_{\text{eff}}}\left[2\left(\tan\psi_{\text{out},2}\frac{\tan\alpha_{\text{tilt},2}}{\tan\alpha_{\text{tilt},1}} + \tan\psi_{\text{in},2}\right)\right. \\
&\quad \left. - \tan\psi_{\text{out},1}\right]\frac{\tan^2\alpha_{\text{tilt},1}}{\tan^2\alpha_{\text{tilt}}} \\
&\quad - \left(\frac{L_{\text{mirror}}}{f_{\text{eff}}} - 1\right)\frac{\tan^2\alpha_{\text{tilt},2}}{\tan^2\alpha_{\text{tilt}}}\tan\alpha_{\text{poc},2} \\
&\quad - \tan\left(\frac{\psi_{\text{defl}}(\Omega_0)}{2}\right)\frac{1}{f_{\text{eff}}^2}\left[\frac{\cos\psi_{\text{out},2}}{\cos\psi_{\text{in},2}}L_{\text{grating}}\frac{\tan\alpha_{\text{tilt},1}}{\tan\alpha_{\text{tilt}}}\right. \\
&\quad \left. - L_{\text{mirror}}\frac{\tan\alpha_{\text{tilt},2}}{\tan\alpha_{\text{tilt}}}\right]^2 .
\end{aligned} \tag{27}$$

and already take into account the flip of orientation at the cylindrical mirror which focuses the laser pulse on the electron trajectory.

3.2.3. Choosing Out-of-Focus Distance and Focusing Distances of the Cylindrical Mirrors

The distance Δf of the interaction point from the focus of the off-axis cylindrical mirror, i.e., the out-of-focus distance, cannot be chosen arbitrarily. Since the interaction point is ahead of the focus the phase fronts of the laser pulse are not plane but bent which leads to a variation of optical undulator frequency during the interaction. This variation must not be too large for TWTS OFEL operation, c.f. Equation (7), and thus there is a minimum out-of-focus distance for TWTS OFELs since phase front curvature reduces with increasing distance from the focus. This assumes Δf is larger than the Rayleigh length of the focused laser pulse which is consistent with the design goal of compact setups. A setup becomes more compact the larger the ratio between laser width at the interaction point and focal width, i.e., the more Rayleigh lengths are between the interaction point and the focus since smaller focal widths allow for shorter focal distances.

The smallest possible Δf can be estimated by approximating the variation in optical undulator frequency $\Delta\tilde{\Omega}$ due to phase-front curvature between start and end of the interaction, which directly depends on Δf, and applying the Limits (7) for TWTS OFEL operation. The variation in undulator frequency is approximated from the instantaneous frequency of a propagating pulse-front tilted laser pulse which is evaluated along the electron trajectory. The electric field of the laser pulse and its instantaneous frequency is derived in **Appendix A**. For the optical undulator frequency variation during the interaction we obtain

$$\frac{\Delta\tilde{\Omega}}{\tilde{\Omega}} = -\frac{L_{\text{int}}}{R_{yz}(\Delta f)}\frac{\sin^2\phi}{(1-\beta\cos\phi)} + \frac{\cos\phi}{4\pi^2\sin^2\phi(1-\beta\cos\phi)}\frac{\lambda_{\text{Laser}}^2}{L_{\text{int}}^2}\,,$$

where $R_{yz}(\Delta f) = \Delta f\left(1 + z_{\text{R,yz}}^2/\Delta f^2\right) \sim \Delta f$ is the phase front curvature of the pulse at the interaction point, $z_{\text{R,yz}}$ the

Rayleigh length of the focused pulse and L_{int} the interaction distance. This approximation assumes a laser pulse width larger than the electron bunch cross-sectional radius σ_{el} and negligibly small group delay dispersion during the interaction which can be accomplished in experiments by precompensation in combination with small interaction angles or exploitation of the plane of optimum compression. The first term in the above expression originates from phase-front curvature and will overshadow the second term originating from the Gouy phase shift in typical TWTS OFEL scenarios with centimeter to meter range interaction distances. The limit for total optical undulator frequency variation is therefore approximated by

$$\left|\frac{\Delta\tilde{\Omega}}{\tilde{\Omega}}\right| = \frac{L_{\mathrm{int}}}{R_{yz}(\Delta f)}\frac{\sin^2\phi}{(1-\beta\cos\phi)} \lesssim 2\rho\,. \tag{28}$$

After rearranging for $R_{yz}(\Delta f)$ and using that the radius of phase-front curvature is always larger than Δf, a condition on the minimum out-of-focus distance is obtained

$$|\Delta f| \gtrsim \frac{L_{\mathrm{int}}}{2\rho}\frac{\sin^2\phi}{(1-\beta\cos\phi)} \approx \frac{\lambda_{\mathrm{Laser}}\sin^2\phi}{2\rho^2(1-\beta\cos\phi)^2} = \frac{L_{\mathrm{int}}^2\sin^2\phi}{2\lambda_{\mathrm{Laser}}}\,, \tag{29}$$

where the last relation on the right-hand side follows from the well-established approximation of the FEL saturation length by about twenty gain length $L_{\mathrm{int}} \approx \lambda_{\mathrm{u}}/\rho$ [45].

Generally, the most compact setups will use the minimum value of Δf since reaching a target laser width w_{yz}, being determined by the required TWTS OFEL interaction length $w_{yz} = L_{\mathrm{int}}\sin\phi$, as close as possible to the actual focus requires a large beam divergence and thus short focal distances. Assuming a linear increase in laser pulse width with distance z from the focus $w_{yz} \approx w_{0,yz}z/z_{\mathrm{R},yz}$, which is valid for $z \gg z_{\mathrm{R},yz} = \pi w_{0,yz}^2/\lambda_{\mathrm{Laser}}$, the laser focal width $w_{0,yz}$ can be approximated by

$$w_{0,yz} = \frac{\lambda_{\mathrm{laser}}\sin\phi}{2\pi\, n_w(1-\beta\cos\phi)\rho}\,, \tag{30}$$

where n_w is a positive number quantifying an increased laser width at the interaction point over the required minimum $L_{\mathrm{int}}\sin\phi$, i.e., $w_{yz} = n_w L_{\mathrm{int}}\sin\phi$, which allows for more compact setups, yet at an increased laser power requirement.

The focusing distances of both cylindrical mirrors in the setup, f_{eff} for the horizontal and f_{el} for the vertical focus, are determined by the respective required widths of the laser pulse, $w_{0,yz}$ and $w_{0,x}$. We use again the linear approximation for pulse width decrease, i.e., for focusing within the interaction plane

$$D_{\mathrm{in}}w_{0,yz} = \lambda_{\mathrm{Laser}}f_{\mathrm{eff}} \tag{31}$$

and for focusing in the vertical direction

$$D_{\mathrm{in}}w_{0,x} = \lambda_{\mathrm{Laser}}f_{\mathrm{el}} \tag{32}$$

where D_{in} is the laser pulse clear aperture before focusing which encloses 99% of the laser pulse power for Gaussian transverse profiles [51].

The focusing distance of the off-axis cylindrical mirror f_{eff} is given by Equations (30) and (31)

$$f_{\mathrm{eff}} = \frac{D_{\mathrm{in}}\sin\phi}{2\pi\, n_w(1-\beta\cos\phi)\rho}\,. \tag{33}$$

The vertical focal width $w_{0,x}$ of the cylindrical mirror, which focuses on the electron trajectory, must match the electron bunch diameter. Assuming a rectangular and uniform transverse laser profile, which allows for a more uniform intensity distribution at the interaction point than a round profile, the focal width needs to be $w_{0,x} = \sqrt{2\pi}\sigma_{\mathrm{el}}$ where σ_{el} is the rms cross-sectional radius of the electron bunch. Thus, using Equation (32), the focal distance is

$$f_{\mathrm{el}} = \frac{\sqrt{2\pi}D_{\mathrm{in}}\sigma_{\mathrm{el}}}{\lambda_{\mathrm{laser}}}\,. \tag{34}$$

For a Gaussian transverse intensity distribution the focal width would be $w_{0,x} = 2\sigma_{\mathrm{el}}$ which overlaps the laser intensity distribution with the electron bunch profile.

3.2.4. Compensating Dispersion at the Interaction Point

The point where spatial dispersion vanishes within the laser path between the off-axis cylindrical mirror, which provides focusing within the interaction plane, and its focal point, is controlled by the residual angular dispersion after the pulse has passed the grating pair. The combination of angular and spatial dispersion before deflection at the off-axis cylindrical mirror provides full control over each frequency's propagation angle and starting position after deflection. This provides full control over pulse-front tilt and spatial dispersion along the propagation path to the focus.

For TWTS OFEL operation spatial dispersion must vanish at the interaction point which is a distance $z_{\mathrm{prop}} = f_{\mathrm{eff}} + \Delta f$ away from the off-axis cylindrical mirror. For an interaction ahead of the focus, the out-of-focus distance Δf is negative. Spatial dispersion is defined as the slope of the linearly approximated distance $y_0(\Omega)$ between a frequency's spatial distribution center and the laser pulse axis

$$SD = \left.\frac{\mathrm{d}y_0}{\mathrm{d}\Omega}\right|_{\Omega=\Omega_0}\,.$$

After deflection at the off-axis cylindrical mirror, it evolves as

$$SD(z) = -\frac{z+f_{\mathrm{eff}}}{\Omega_0}\tan\alpha_{\mathrm{tilt}} + SD_{\mathrm{in}}\,, \tag{35}$$

where $z = 0$ marks the off-axis cylindrical mirror focus. This expression takes reflection at the second cylindrical mirror, and the corresponding change of sign, already into account. Spatial dispersion of the pulse before deflection at the off-axis cylindrical mirror is

$$SD_{\mathrm{in}} = \frac{\cos\psi_{\mathrm{out},2}}{\cos\psi_{\mathrm{in},2}}\frac{L_{\mathrm{grating}}}{\Omega_0}\tan\alpha_{\mathrm{tilt},1} - \frac{L_{\mathrm{mirror}}}{\Omega_0}\tan\alpha_{\mathrm{tilt},2}\,. \tag{36}$$

SD_{in} and the pulse-front tilt $\alpha_{\mathrm{tilt},2}$ after the grating pair must be adjusted with the grating pair and the propagation distance L_{mirror} to the off-axis cylindrical mirror in order to ensure both correct pulse-front tilt $\alpha_{\mathrm{tilt}} = \phi/2$ of half the interaction angle and vanishing spatial dispersion $SD(\Delta f) = 0$ at the interaction point. Using Equation (35) the latter requirement sets the target value for spatial dispersion before deflection at the off-axis cylindrical mirror

$$SD_{\mathrm{in,target}} = \frac{\Delta f + f_{\mathrm{eff}}}{\Omega_0} \tan(\phi/2)\,. \tag{37}$$

The target value for pulse-front tilt after the second grating is obtained by recasting Equation (27) for pulse-front tilt at the interaction point into an expression for $\alpha_{\mathrm{tilt},2}$, additionally making use of (36) and inserting (37)

$$\tan\alpha_{\mathrm{tilt,2,target}} = -\tan(\phi/2)\frac{\Delta f}{f_{\mathrm{eff}}}\,. \tag{38}$$

If L_{mirror} and $L_{\mathrm{grating,eff}} = (\cos\psi_{\mathrm{out},2}/\cos\psi_{\mathrm{in},2})L_{\mathrm{grating}}$ shall remain free parameters such that they can be adjusted to fit specific lab conditions, the desired design value for pulse-front tilt after the first grating $\alpha_{\mathrm{tilt},1}$ is predetermined as well

$$\tan\alpha_{\mathrm{tilt,1,target}} = \frac{\Delta f\left(1 - L_{\mathrm{mirror}}/f_{\mathrm{eff}}\right) + f_{\mathrm{eff}}}{L_{\mathrm{grating,eff}}} \tan(\phi/2)\,, \tag{39}$$

which is obtained again from the first equation in (27).

Vanishing group delay dispersion GDD at the interaction point is accomplished by providing an input pulse with negative group delay dispersion, i.e., a laser pulse being either uncompressed or not fully compressed by the laser compressor. The absolute GDD value of the input pulse must match GDD_0 which is introduced by the grating pair and propagation with pulse-front tilt

$$\begin{aligned} GDD_0 = \frac{1}{\Omega_0 c}\big(&L_{\mathrm{grating}}\tan^2\alpha_{\mathrm{tilt},1} + L_{\mathrm{mirror}}\tan^2\alpha_{\mathrm{tilt},2} \\ &+(f_{\mathrm{eff}} + \Delta f)\tan^2(\phi/2)\big)\,, \end{aligned} \tag{40}$$

where again $\Delta f < 0$ for an interaction before the focus, as in all of the above equations.

Moreover, the requirement of an aberration-free pulse demands a large f-number $f/\# = f/D_{\mathrm{in}} \gg 1$ at the off-axis cylindrical mirror as otherwise angular dispersion of the incident pulse results in coma.

3.2.5. Obtaining Parameters of the Out-of-Focus Interaction Setup

By now all fixed parameters of out-of-focusing setups are determined. These are pulse-front tilt after first and second grating, $\tan\alpha_{\mathrm{tilt,1,target}}$ and $\tan\alpha_{\mathrm{tilt,2,target}}$ respectively, the effective focal distance of the off-axis cylindrical mirror f_{eff}, the focal distance of the cylindrical mirror f_{el}, and the out-of-focus distance Δf.

The parameters left to be determined are first grating incidence angle $\psi_{\mathrm{in},1}$ and line density n_1, effective distance between the gratings $L_{\mathrm{grating,eff}}$, second grating rotation angle ϵ and line density n_2, the distance between second grating and off-axis cylindrical mirror L_{mirror} as well as the off-axis cylindrical mirror deflection angle ψ_{defl}.

Out of these the first grating parameters $(\psi_{\mathrm{in},1}, n_1)$ can be determined in dependence of the other parameters which can be chosen to accommodate with e.g., lab space or components available on-stock. The defining equations for first grating parameters are

$$\begin{aligned} \tan\psi_{\mathrm{out},1} = \Bigg\{ &2\frac{L_{\mathrm{grating,eff}}}{f_{\mathrm{eff}}}\left(\tan\psi_{\mathrm{out},2}\frac{\tan\alpha_{\mathrm{tilt,2,target}}}{\tan(\phi/2)}\right. \\ &\left.+\tan\psi_{\mathrm{in},2}\frac{\tan^2\alpha_{\mathrm{tilt,1,target}}}{\tan^2(\phi/2)}\right) \\ &-\tan\left(\frac{\psi_{\mathrm{defl}}(\Omega_0)}{2}\right)\frac{1}{f_{\mathrm{eff}}^2}\left[L_{\mathrm{grating,eff}}\frac{\tan\alpha_{\mathrm{tilt,1,target}}}{\tan(\phi/2)}\right. \\ &\left.-L_{\mathrm{mirror}}\frac{\tan\alpha_{\mathrm{tilt,2,target}}}{\tan(\phi/2)}\right]^2 \\ &+\operatorname{cotan}\phi \\ &-\left(\frac{L_{\mathrm{mirror}}}{f_{\mathrm{eff}}} - 1\right)\left(\frac{\sin\psi_{\mathrm{in},2}}{\cos\psi_{\mathrm{out},2}}\frac{\tan^2\alpha_{\mathrm{tilt,1,target}}}{\tan^2(\phi/2)}\right. \\ &\left.-\tan\psi_{\mathrm{out},2}\frac{\tan^2\alpha_{\mathrm{tilt,2,target}}}{\tan^2(\phi/2)}\right)\Bigg\} \\ &\Bigg/\left[\frac{L_{\mathrm{grating,eff}}}{f_{\mathrm{eff}}}\frac{\tan^2\alpha_{\mathrm{tilt,1,target}}}{\tan^2(\phi/2)}\right. \\ &\left.+\left(\frac{L_{\mathrm{mirror}}}{f_{\mathrm{eff}}} - 1\right)\frac{\tan^2\alpha_{\mathrm{tilt,1,target}}}{\tan^2(\phi/2)}\frac{\cos\psi_{\mathrm{in},2}}{\cos\psi_{\mathrm{out},2}}\right] \end{aligned} \tag{41}$$

$$\sin\psi_{\mathrm{in},1} = \cos\psi_{\mathrm{out},1}\tan\alpha_{\mathrm{tilt,1,target}} + \sin\psi_{\mathrm{out},1}\,, \tag{42}$$

where the equation for first grating diffraction angle (42) is obtained by rearranging the relation for plane of optimum compression orientation in Equation (27). The equation for first grating incidence angle (42) ensures correct pulse-front tilt $\alpha_{\mathrm{tilt},1} = \alpha_{\mathrm{tilt,1,1target}}$ after the first grating. In order to ensure correct pulse-front tilt $\alpha_{\mathrm{tilt},2} = \alpha_{\mathrm{tilt,2,target}}$ after the second grating, the second grating incidence and diffraction angles, $\psi_{\mathrm{in},2}$ and $\psi_{\mathrm{out},2}$ respectively, need to fulfill the condition

$$\begin{aligned} 0 = &\frac{\sin\psi_{\mathrm{in},2} - \sin\psi_{\mathrm{out},2}}{\cos\psi_{\mathrm{out},2}} - \frac{\cos\psi_{\mathrm{in},2}}{\cos\psi_{\mathrm{out},2}}\tan\alpha_{\mathrm{tilt,1,target}} \\ &-\tan\alpha_{\mathrm{tilt,2,target}}\,. \end{aligned} \tag{43}$$

An initial choice of second grating parameters may be driven by the requirement of high diffraction efficiency. However, this initial choice may need to be refined in order to accommodate resultant requirements on the setup, e.g., to attain a feasible distance between the gratings or to adapt the first grating parameters to those of on-stock available gratings.

In general, the first grating parameters will be equal or similar to those of the second grating since the pulse-front tilt after the second grating $\tan\alpha_{\mathrm{tilt,2,target}}$ is proportional to $\Delta f/f_{\mathrm{eff}} =$

$\pi w_{0,yz}/D_{\text{in}} \ll 1$ which is a small quantity. If it were not small, focusing would be omitted, since in this case $w_{0,yz} \sim D_{\text{in}}$, and the setup without focusing within the interaction plane may be used.

3.2.6. Limits on Variations in Laser Pulse Properties and Optical Setup Parameters for TWTS OFEL Operation

As before, misalignment of the optical components leads to optical undulator amplitude and frequency variations during the interaction due to the deviation of plane of optimum compression and pulse-front tilt orientation. For the setup including focusing within the interaction plane, these are induced by a variation in one of the parameters $(\psi_{\text{in},1}, \epsilon, L_{\text{grating}}, L_{\text{mirror}}, f_{\text{eff}}, \Delta f)$ via Relations (27). Variations in plane of optimum compression and pulse-front tilt orientation, $\Delta \tan\alpha_{\text{poc}}$ and $\Delta \tan\alpha_{\text{tilt}}$ respectively, are connected to optical undulator amplitude and frequency variations via Relations (20), (21), and (25) again, which assumes the pulse is dispersion free along the electron trajectory for exact alignment.

The out-of-focus interaction may also induce variations of optical undulator amplitude due to pulse-front curvature. This variation can be estimated from the term including the expression describing overlap of electrons and laser pulse $\tilde{L}'$ in the normalized intensity distribution of the defocusing laser pulse, cf. Equation (47),

$$\frac{I(y,z,t)}{I(0,0,0)} = \mathrm{e}^{-2\tilde{L}'^2},$$

where

$$\tilde{L}' = \frac{ct + \Delta f - z + y\tan\alpha_{\text{tilt}} - y^2/(2R)}{c\tau_0}.$$

In order to obtain the estimate, this expression is evaluated along the electron trajectory (19) which needs to be relocated to $z = \Delta f$ at $t = 0$. At the end of the interaction ($t_{\text{end}} = L_{\text{int}}/2c$), the intensity variation due to pulse-front curvature can be estimated by

$$\left|\frac{\Delta I}{I}\right| = \Delta\tilde{L}'^2 = \left(\frac{L_{\text{int}}^2 \sin^2\phi}{8c\tau_0\Delta f}\right)^2,$$

which is limited by the first of Equation (7) for TWTS OFEL operation. Since percent level laser intensity variations are typically acceptable for TWTS OFEL operation, this constraint on the setup parameters is not as strict as the constraint set by undulator frequency variation caused by phase-front curvature (28), which was used to derive the minimum out-of-focus distance. Thus the influence of pulse-front curvature will be usually negligible. In case it is not, the out-of-focus distance Δf needs to be increased.

4. EXAMPLES OF A HIGH-YIELD INCOHERENT TWTS SOURCE AND TWTS OFELs

Here, we present examples of a yield-enhanced Thomson X-ray source by TWTS as well as TWTS OFELs emitting at vacuum ultraviolet (VUV), extreme ultraviolet (EUV) and X-ray wavelengths. Their electron and laser pulse requirements are provided and parameters of the optical setups as well as alignment tolerances are determined. Thereby we demonstrate the usage of the formulas derived in the last two sections. The examples show that the requirements and optical setup parameters of enhanced Thomson sources and VUV TWTS OFELs are technically feasible such that these sources can be realized today.

In order to complement our analytical approach for the determination of setup parameters, we also modeled the optical setup of the first example in ZEMAX which traces rays through it without approximations [52]. It allows validating the correctness of the orientations of pulse front and plane of optimum compression at the interaction point. According to Equation (3), time delay (*TD*) and group delay dispersion (*GDD*) are constant within these planes, respectively, where

$$TD = \left.\frac{\mathrm{d}\varphi}{\mathrm{d}\Omega}\right|_{\Omega=\Omega_0} \qquad GDD = \left.\frac{\mathrm{d}^2\varphi}{\mathrm{d}\Omega^2}\right|_{\Omega=\Omega_0}.$$

With ZEMAX *TD* and *GDD* can be sampled along planes which are expected to overlap with the pulse-front or the plane of optimum compression, with the expected orientations given by the analytical Relations (9) and (10). Time delay and group delay dispersion are calculated in ZEMAX from the optical path lengths of three different wavelengths λ_i propagating through the setup, where $\lambda_2 < \lambda_1 = \lambda_{\text{Laser}} < \lambda_3$ and $(\lambda_3 - \lambda_2)/(2\lambda_1) \ll 1$. The optical path length OPTH of a wavelength is provided by the equally named function of the ZEMAX Programming Language ZPL. The optical path lengths OPTH_i of wavelengths λ_i $(i = 1, 2, 3)$ are used to calculate the phases $\varphi_i = \frac{2\pi}{\lambda_i}\text{OPTH}_i$ from which time delay and group delay dispersion are computed by numerical differentiation

$$TD = \frac{\varphi_3 - \varphi_2}{2(\lambda_1 - \lambda_2)}\left(-\frac{2\pi c}{\Omega_0^2}\right)$$
$$GDD = \frac{\varphi_3 - 2\varphi_1 + \varphi_2}{(\lambda_1 - \lambda_2)^2}\left(\frac{2\pi c}{\Omega_0^2}\right)^2 - \frac{2}{\Omega_0}TD. \qquad (44)$$

The macro calculating *TD* and *GDD* is presented in **Appendix B**.

4.1. Incoherent Hard X-Ray TWTS Source

In Steiniger et al. [31], it is shown that a hard X-ray source radiating 30 keV photons reaches about a fifty-times higher spectral photon density when realized in a $\phi = 120°$ TWTS geometry instead of a head-on Thomson scattering geometry. While both setups utilize the same laser system and electron source, the optimized overlap of electrons and laser pulse in the TWTS geometry provides for an increase of optical undulator length and a reduction of optical undulator strength compared to the head-on geometry resulting in this significant increase of spectral photon density. In these setups, the laser is a typical Ti:sapphire system with $\lambda_{\text{Laser}} = 800$ nm, $\tau_{\text{FWHM,I}} = 25$ fs full duration at half maximum of the intensity profile and 1 J pulse energy. It provides a total interaction distance of 42 mm at an undulator strength $a = 0.03$ in the $\phi = 120°$ TWTS geometry.

The large interaction angle and the correspondingly large pulse-front tilt $\alpha_{\text{tilt}} = 60^\circ$ require dispersion compensation during the interaction as the pulse would otherwise elongate to $116\tau_{\text{FWHM,I}}$ during the interaction, if optimum compression is ensured only in the middle of the interaction. In accordance with **Figure 2B** the orientation of the plane of optimum compression is $\alpha_{\text{poc}} = 30^\circ$. The procedure described in paragraph 3.1.2 is used to determine the grating parameters.

In the following, we determine the parameters of the gratings which are used to operate this incoherent hard X-ray TWTS light source. In essence, second grating parameters $(\psi_{\text{in},2}, n_2)$ ensuring correct orientation of pulse-front tilt and plane of optimum compression are determined for a range of first grating parameters $(\psi_{\text{in},1}, n_1)$ using the coupled Equation (12). Then the grating pair promising best diffraction efficiency is chosen.

In detail, the equations

$$\sin\psi_{\text{in},2} = s_{\text{i}}(s_{\text{o}}, \psi_{\text{in},1}, n_1, \phi) \quad \sin\psi_{\text{out},2} = s_{\text{o}}(s_{\text{i}}, \psi_{\text{in},1}, n_1, \phi)\,,$$

which stem from (12), form a system of implicit equations for the second grating parameters $(\psi_{\text{in},2}, \psi_{\text{out},2})$. A solution to this system ensures correct orientation of plane of optimum compression and pulse-front tilt for a first grating parameter pair and an interaction angle ϕ. A second grating incidence angle, which is a solution to the system, is a root of the implicit function $\sin\psi_{\text{in},2} - s_{\text{i}}(s_{\text{o}}(\sin\psi_{\text{in},2}, \psi_{\text{in},1}, n_1, \phi), \psi_{\text{in},1}, n_1, \phi) = 0$, and is found by scanning through the range $\psi_{\text{in},2} \in [-90^\circ, 90^\circ]$ for some arbitrarily chosen first grating parameters and the given interaction angle. The range of possible first grating parameters is defined by the existence of a root to this implicit function and the requirement of diffraction only into −1st order. For this example, the usable range of first grating line densities is about $n_1 \in [1200\,\text{l/mm}, 1500\,\text{l/mm}]$ with angles close to normal incidence.

Out of this range of possible first grating line densities, the largest $n_1 = 1500\,\text{l/mm}$ is chosen for a first iteration in order to maximize the generation of spatial dispersion during propagation between the gratings. This spatial dispersion is a precompensation for spatial dispersion generated during propagation from the second grating to the interaction region. The scaling of second grating line density and incidence angle with first grating incidence angle for this first grating line density is shown in **Figures 8A,B**, respectively. In order to ensure a high diffraction efficiency for the second grating, a line density $n_2 = 2300\,\text{l/mm}$ is chosen since it allows for a second grating incidence angle close to the grating's Littrow angle. The exact angles of first grating incidence $\psi_{\text{in},1}$ and second grating rotation ϵ belonging to this set of chosen line densities are determined from the scaling of required pulse-front tilt $\alpha_{\text{tilt}} = 60^\circ$ and plane of optimum compression $\alpha_{\text{poc}} = 30^\circ$ depicted in **Figure 8C**. At $(\psi_{\text{in},1} = 16.635^\circ, \epsilon = -7.043^\circ)$ both pulse-front tilt and plane of optimum compression have correct orientation for TWTS ensuring continuous overlap of electrons and laser pulse as well as full dispersion compensation.

An optical setup utilizing these gratings to realize a 120° TWTS source is shown in **Figure 9**. A laser pulse of 50 mm diameter enters the grating arrangement, diffracts twice and propagates to a planar mirror where it is redirected to the cylindrical mirror. It focuses the pulse vertically to 50 µm full width at half maximum of the intensity profile corresponding to the electron bunch width. The laser propagation distance L_{prop} from the first grating to the interaction point is 3.3 m. Thereby the propagation distances between first and second grating, second grating and planar mirror, as well as planar and cylindrical mirror are kept small in order to obtain a compact setup. Most of the propagation distance is required for vertical focusing. Reducing the vertical laser pulse diameter from 50 mm to 50 µm requires a cylindrical mirror of 2.5 m focal distance. The laser pulse actually travels a distance of 2.9 m to the line focus since the laser pulse direction of propagation and the mirror's surface normal enclose an angle of 30°.

During propagation from the second grating to the interaction point, the laser pulse width increases significantly due to spatial dispersion. It becomes large due to large angular dispersion which is necessary to provide the large pulse-front tilt. Spatial dispersion can be countervailed by increasing the propagation distance between first and second grating, by passing through an additional upstream grating pair of two equal gratings or by using varied line-space gratings [30].

With ZEMAX first and second order dispersion, *TD* and *GDD* respectively, are sampled multiple times in planes oriented along the expected orientations of pulse-front and plane of optimum compression, respectively. Expectations stem from our respective analytic Relations (9) and (10). The sampling shows excellent agreement between the analytic formulas and ray tracing in ZEMAX, (cf. **Table 1**), which validates our analytic model. The difference in time delay of 1.5 fs amounts to a deviation of the pulse-front tilt angle by 30 µrad resulting in a 1% intensity fluctuation during the interaction, according to Equations (17), (18) and assuming full pulse compression in the middle of the interaction. The difference in group delay dispersion of $8\,\text{fs}^2$ amounts to a prolongation of the pulse duration by 0.04 per mill during the interaction, assuming spatial and group delay dispersion are fully compensated in the middle of the interaction. The *GDD* value obtained from ZEMAX thereby represents the required amount of precompensation.

This example of an enhanced Thomson source by TWTS proves the feasibility of the Traveling-Wave Thomson-Scattering geometry as well as the applicability of the analytic equations derived to determine the grating parameters. The optical components of this setup are available allowing for the realization of this or similar enhanced Thomson sources today. Important aspects in a successful implementation of an enhanced Thomson source are sufficient synchronization of electron bunch and laser pulse on the level of the longer of the two pulse durations as well as the development of diagnostics to analyze plane of optimum compression and pulse-front tilt orientation in the line focus. Synchronization on the sub-100 fs level has been demonstrated already [53] and can be sufficient for conventionally accelerated electrons. Laser wakefield acceleration of electrons offers inherent synchronization when a single laser pulse is split in two where one drives the electron acceleration and the other provides the optical undulator. Developing diagnostics is especially relevant when an enhanced Thomson source

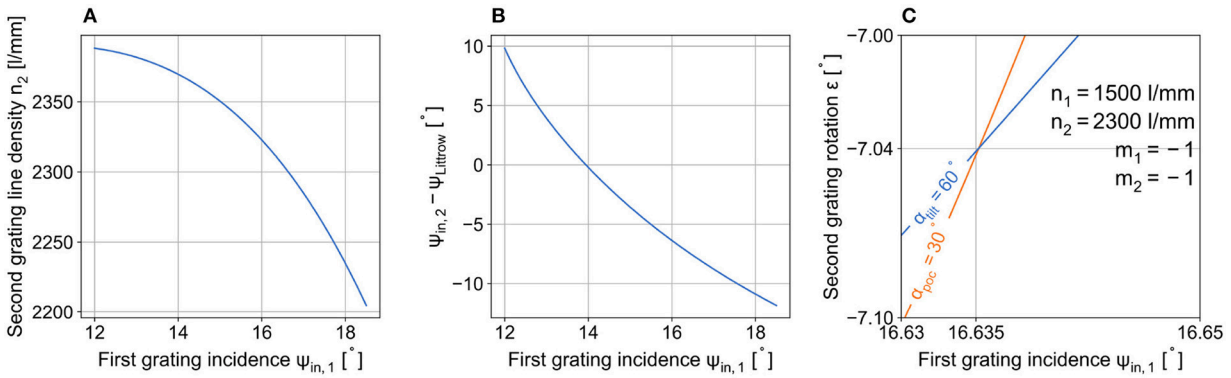

FIGURE 8 | Scaling of **(A)** second grating line density n_2 and **(B)** incidence angle $\psi_{in,2}$ to ensure correct orientation of plane of optimum compression and pulse front tilt in dependence of first grating incidence angle $\psi_{in,1}$ at line density $n_1 = 1500$ l/mm for the $\phi = 120°$ incoherent TWTS source. The incidence angle at the second grating is measured relative to its Littrow angle $\psi_{Littrow}$. **(C)** Determining second grating rotation angle and first grating incidence angle for a second grating line density of $n_2 = 2300$ l/mm. Solid lines connect pairs $(\psi_{in,1}, \epsilon)$ which leave the orientation of pulse-front tilt (blue) or plane of optimum compression (orange) constant. Both gratings diffract into −1st order, i.e., $m_1 = m_2 = -1$.

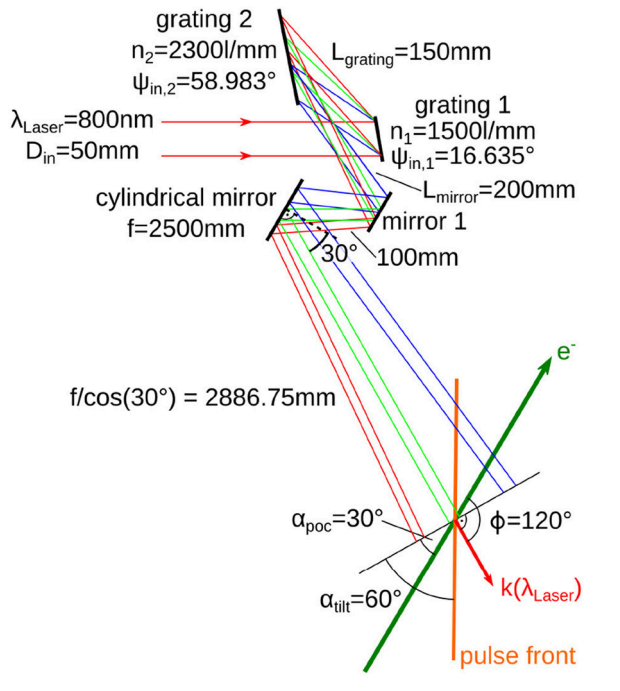

FIGURE 9 | Optical setup of an incoherent, hard X-ray TWTS source operating at $\phi = 120°$ interaction angle. Rays of different color represent paths taken by different wavelengths of the 80 nm wide laser pulse spectrum, where blue, green and red correspond to wavelengths of 760 , 800, and 840 nm, respectively. A laser pulse of 50 mm width enters the setup from the left and first passes a grating pair to adjust its angular dispersion and group delay dispersion according to the requirements for correct pulse front tilt $\alpha_{tilt} = 60°$ and plane of optimum compression orientation $\alpha_{poc} = 30°$. After subsequent reflection at the planar mirror and focusing in the vertical direction to a width of 50 μm by the cylindrical mirror, the laser pulse interacts with the electrons.

TABLE 1 | ZEMAX calculation of time delay and group delay dispersion for the $\phi = 120°$ incoherent TWTS source in the setup without focusing within the interaction plane.

Time delay *TD* sampled along pulse front	**Absolute [ps]**	**Relative to center [fs]**
Left edge	17801.4909	+1.5
Center	17801.4894	0
Right edge	17801.4879	−1.5

Group delay dispersion *GDD* sampled during interaction	**Absolute [ps^2]**	**Relative to middle [fs^2]**
Begin	−15.401934	−8
Middle	−15.401926	0
End	−15.401918	+8

Time delay and group delay dispersion are sampled at three different positions along the pulse-front and electron trajectory, respectively. Time delay is nearly constant at left edge, center and right edge along the plane $z = \tan(60°)y$ agreeing with the expected pulse-front tilt of $\alpha_{tilt} = 60°$. Group delay dispersion is almost constant at begin, middle and end of the interaction along the electron trajectory $z = \tan(30°)y$ agreeing with the expected orientation of plane of optimum compression $\alpha_{poc} = 30°$. The absolute value of GDD in the middle of the interaction represents the required precompensation for optimum laser pulse duration during the interaction.

represents an intermediate step toward the realization of a TWTS OFEL where overlap and good optical undulator quality must be established, controlled and maintained over centimeter scale interaction distances to drive the FEL instability. Setups for a VUV, an EUV, and an X-ray TWTS OFEL are presented in the following.

4.2. VUV and EUV TWTS OFELs

A vacuum ultraviolet (VUV) TWTS OFEL providing intense and ultrashort radiation pulses at 100 nm wavelength is realizable today. Laser systems and electron accelerators providing laser pulses and electron bunches of necessary quality exist already. Besides serving as a demonstrator for TWTS OFEL operation, a VUV TWTS OFEL has applications e.g., to the study of ionization dynamics in nonlinear, high-intensity laser interaction

with matter [54], to observe reaction kinetics at surfaces [55, 56], to study ablation from materials surfaces [57] or to seed shorter wavelengths FELs. EUV TWTS OFELs providing ultra-short coherent radiation pulses at an extreme ultraviolet (EUV) wavelength of 13.5 nm have applications for example in 3D structure determination of nanoscale objects [58] or in imaging ultra-fast transient, nanoscale dynamics [59]. High yield EUV sources are also applied in materials science [60, 61] and are demanded by the semiconductor industry [62]. Compared to existing large scale conventional FEL facilities such as FLASH [63] or FERMI@Elletra [64] a TWTS OFEL is a potentially more compact source due to the lower electron energy and shorter interaction distance. As a consequence thereof, TWTS OFELs produce fewer photons than these large-scale machines. Yet they can achieve orders of magnitude higher photon yield and brilliance than incoherent sources [32].

Determining laser, electron and setup parameters of VUV and EUV TWTS OFELs requires to combine the scaling laws for the setup including focusing within the interaction plane given in section 3.2 and the scaling laws for electron bunch and laser pulse requirements for TWTS OFELs given by Steiniger et al. [31]. Usage of the out-of-focus setup is explained after the discussion of the OFEL parameters.

4.2.1. Choosing Electron and Laser Parameters

In these examples the optical undulator is provided by a petawatt laser system operating at 1035 nm central wavelength and electrons are assumed to have an energy of 15 and 22 MeV(EUV) as well as a peak current of 0.8 and 1.5 kA(EUV) for the VUV and EUV TWTS OFEL, respectively. The interaction angles are set to $\phi = 10.1°$(VUV) and $\phi = 12.1°$(EUV).

The choice of electron energies and interaction angles represent a trade-off between several opposed scalings. For example, while the acceptable relative electron bunch energy spread increases with smaller interaction angles for a target wavelength, as represented by the scaling of the Pierce parameter

$$\rho \propto (1 - \beta \cos\phi)^{-1/6} \lambda_{\mathrm{FEL}}^{1/2}, \tag{45}$$

at the same time smaller interaction angles increase the size of the setup, as is seen from the scaling of the laser propagation distance from the off-axis cylindrical mirror to the interaction point

$$z_{\mathrm{prop}} = f_{\mathrm{eff}} - \left|\Delta f\right| \approx f_{\mathrm{eff}} \propto \frac{\sin\phi}{(1 - \beta\cos\phi)^{5/6}} \lambda_{\mathrm{FEL}}^{-1/2}.$$

Furthermore, the interaction angle should not become too small, typically larger than about 3°, since smaller interaction angles increase the projected size of the laser pulse on the cylindrical mirror, which focuses in the vertical direction, into the meter scale requiring meter scale cylindrical mirrors. Another example is the requirement on normalized electron bunch emittance originating from electron bunch divergence. Electron divergence results, on the one hand, in a loss of overlap with the laser pulse during the interaction. On the other, in radiation bandwidth increase from the difference in interaction angles between electrons. Upper limits on acceptable emittance derived from loss of overlap and bandwidth increase, respectively, show opposed scaling. For TWTS OFEL operation the stronger of the limits needs to be fulfilled and thus parameters of the OFEL need to be chosen carefully to stay within today achievable requirements. Further trade-offs need to made when choosing, for example, optical undulator strength a or electron bunch rms cross-sectional radius which will be mostly influenced by balancing the requirements on laser power and intensity stability. The final choice of electron and laser parameters is shown in **Table 2**.

TABLE 2 | Parameters and requirements of electrons and laser pulse for TWTS OFELs radiating at 100 nm, 13.5 nm and 1.5 Å.

Electron and optical undulator parameters	VUV TWTS OFEL w/ focusing	EUV TWTS OFEL w/ focusing	Å TWTS OFEL w/o focusing
Resonant wavelength λ_{FEL} [nm]	100	13.5	0.15
Interaction angle ϕ [°]	10.1	12.1	7
Undulator wavelength λ_u [μm]	65	46	139
Electron energy E_{el} [MeV]	15	22	349
Peak current I_{p} [kA]	0.8	1.5	5
Electron bunch charge [pC]	350	350	350
Electron bunch duration (rms) $\sigma_{\mathrm{t,b}}$ [fs]	175	93	28
Electron bunch rms radius σ_{b} [μm]	7	10	10
Norm. transv. emittance ϵ_{n} [mm mrad]	0.5	0.5	0.2
Rel. energy spread $\sigma_{\mathrm{E}}/E_{\mathrm{el}}$	0.8%	0.2%	0.02%
Undulator parameter a	2	0.5	0.17
Minimum laser peak power for OFEL [TW]	890	283	576
Transv. intensity profile stability	2.5%	3.6%	2.8%
Gain length [mm]	0.35	1	32
Interaction distance L_{int} [cm]	0.57	1.68	51.0
Peak radiation power [MW]	104	68	350
Number of Photons	2×10^{13}	1×10^{12}	2×10^{10}

The 1.5 Å TWTS OFEL uses the setup without focusing within the interaction plane, ***Figure 6****, while the VUV and EUV TWTS OFEL use the setup providing focusing within the interaction plane,* ***Figure 3****.*

High brilliance electron bunches with parameters suitable for VUV TWTS OFEL operation can be provided by state-of-the-art conventional thermionic- or photoinjectors [65–71]. These routinely provide electron bunches of 0.5–1 mm mrad normalized transverse emittance and 20 keV ps-level longitudinal emittance at a few hundred picocoulomb charge. This is in agreement with the emittance requirements of the example of $\epsilon_{\mathrm{n}} = 0.5\,\mathrm{mm\,mrad}$ and $\epsilon_{\mathrm{long}} \propto \sigma_{\mathrm{E}}\sigma_{\mathrm{t,b}} = 21\,\mathrm{keV\,ps}$. Well established techniques allow to maintain these low emittances during acceleration to gigaelectronvolt final energies and compression to kiloampere currents [63, 66, 72]. For the

EUV TWTS OFEL the increased energy spread of the bunch after acceleration and compression can be reduced again by e.g., corrugated structures [73, 74] to meet the requirements.

4.2.2. Choosing Optical Setup Parameters

In view of the centimeter-scale interaction distances the advantage of using the out-of-focus setup becomes clear. With $L_{\mathrm{int}} = 16.8\,\mathrm{mm}$ for the EUV TWTS OFEL a millimeter-scale laser pulse width of $w = L_{\mathrm{int}} \sin\phi = 3.5\,\mathrm{mm}$ is required at the interaction point. For example, assuming a laser system with $\tau_{\mathrm{FWHM,I}} = 120\,\mathrm{fs}$ pulse duration, which provides good longitudinal overlap of electrons and laser pulse, the required pulse energy is 34 J to reach the target laser power of 283 TW corresponding to an optical undulator strength of $a = 0.5$. This requires a pulse diameter of $D_{\mathrm{in}} = 9.5\,\mathrm{cm}$ before focusing to keep the areal energy density of the pulse below $0.4\,\mathrm{J/cm^2}$ in order to avoid damage on optics. If an in-focus interaction geometry is used, the focusing distance would be 324 m.

Utilizing the out-of-focus geometry, the effective focal distance for horizontal focusing within the interaction plane is reduced to 70 m and the out of focus distance is −8.2 m, which is obtained by Equations (31) and (29) respectively. But the focusing distance can be further reduced by a factor of two by employing a one petawatt laser system with 120 J energy per pulse. The higher power allows to let the pulse interact with the electrons at a distance from the focus where its width is still larger than required to provide the interaction distance. Using such an oversized pulse at the interaction point allows employing stronger focusing which reduces the effective focal distance. For the EUV TWTS OFEL the oversize factor can be $n_w = 3.6$ with a petawatt laser pulse which decreases the effective focal distance to $f_{\mathrm{eff}} = 35.854\,\mathrm{m}$. The out of focus distance becomes $\Delta f = -8.170\,\mathrm{m}$ resulting in a total propagation distance of $z_{\mathrm{prop}} \approx 28\,\mathrm{m}$ from the off-axis cylindrical mirror to the interaction point. This is a significant size reduction compared to the 324 m focusing distance of an in-focus interaction setup at equal interaction angle.

In order to keep the energy fluence on optics below $0.4\,\mathrm{J/cm^2}$ the higher-power laser pulse is assumed to have a larger diameter of $D_{\mathrm{in}} = 175\,\mathrm{mm}$.

Before the laser pulse is focused it passes through the grating setup and covers the distance to the off-axis cylindrical mirror. During this propagation, the required spatial dispersion and pulse-front tilt need to be generated. We assume the effective grating separation distance is set to $L_{\mathrm{eff}} = 2.5\,\mathrm{m}$, the distance between second grating and off-axis cylindrical mirror is set to $L_{\mathrm{mirror}} = 2\,\mathrm{m}$ and the deflection angle at the mirror is set to $\psi_{\mathrm{defl}} = 15^\circ$ for the EUV TWTS OFEL. Then, the required pulse-front tilt after first and second grating is $\alpha_{\mathrm{tilt},1} = 50.029^\circ$ and $\alpha_{\mathrm{tilt},2} = 1.383^\circ$, respectively, which is obtained by Equations (39) and (38). The corresponding grating parameters are determined in the following.

First, initial values for second grating line density n_2 and incidence angle $\psi_{\mathrm{in},2}$ are determined by Equation (43), which ensures correct pulse-front tilt after the second grating. Comparing the required incidence angle with the grating's Littrow angle for several line densities shows that a feasible line density, where the required incidence angle is close but not too close to the Littrow angle ψ_{Littrow}, is $n_2 = 1040\,\mathrm{l/mm}$ with $\psi_{\mathrm{in},2} = 27.59^\circ$ and $\psi_{\mathrm{Littrow}} = 32.56^\circ$.

Second, Equations (41) and (42) are used to determine an initial value for first grating incidence angle and line density of $\psi_{\mathrm{in},1} = 25.77^\circ$ and $n_1 = 957.7\,\mathrm{l/mm}$, respectively.

Third, the first grating line density is rounded to a practical value of $n_1 = 960\,\mathrm{l/mm}$. In order to yield the correct pulse-front tilt after first and second grating the incidence angles have to be determined again using Equation (9) and its counterpart for diffraction at a single grating. The new incidence angles are $\psi_{\mathrm{in},1} = 26.36^\circ$ and $\psi_{\mathrm{in},2} = 27.263^\circ$.

All parameters of the setup are determined by now. If they are not satisfactory, e.g., the incidence angle at the first grating could be too far from its Littrow angle resulting in low diffraction efficiency, or the initially chosen grating separation distance is too short such that parts of the setup block the beam path, another iteration of the above steps can be done with different choices for $L_{\mathrm{grating,eff}}$, L_{mirror}, ψ_{defl} or n_2. None of the above reasons applies to this EUV TWTS OFEL setup. **Table 3** lists the complete set of optical setup parameters and alignment tolerances for the VUV and EUV TWTS OFELs.

The alignment tolerances are all reachable with current technical standards. The smaller acceptable tolerances of the EUV TWTS OFEL originate from its longer interaction distance due to which an alignment error results in a larger separation of electrons and laser pulse at the end of interaction. The most delicate aspect is the first grating incidence angle with an acceptable variation of $\Delta\psi_{\mathrm{in},1} = 2.8\,\mathrm{mrad}$ for the EUV TWTS OFEL, if all other components are optimally aligned. However, this should not be an obstacle as for high power laser systems microradian grating alignment accuracy has been achieved [75–77]. The acceptable variation in distance between the second grating and the off-axis cylindrical mirror is on the meter scale since the pulse-front tilt after the grating pair is only about 1° and thus the change in spatial dispersion during propagation is very small.

These designs show that TWTS OFELs can be realized today by currently available accelerators and laser systems. They are able to reduce the size of free-electron lasers to the scale of a lab hosting a petawatt-class laser since the optical undulator periods and interaction lengths for TWTS OFELs are orders of magnitude smaller than at conventional free-electron lasers. The final focusing of the laser pulse to a millimeter scale width takes most of the space on a scale equal to the total length of a magnetic undulator section at a conventional EUV free-electron laser. Yet this space is only in-vacuum laser propagation distance without any laser optics inside and independent of the electron beam transport system. Together with the smaller electron energy and thus smaller accelerator, this will still result in an order of magnitude reduction of facility size compared to conventional free-electron lasers utilizing magnetic undulators. A further reduction of the setup size becomes possible by using an asymmetric transverse pulse profile with large aspect ratio allowing to equalize the horizontal and vertical focusing distances.

TABLE 3 | Optical components parameters for the 100 and 13.5 nm TWTS OFEL in the setup providing focusing within the interaction plane visualized in **Figure 6**.

Optical setup parameters	VUV TWTS OFEL w/ focusing	EUV TWTS OFEL w/ focusing
Laser wavelength λ_{Laser} [μm]	1.035	1.035
Laser pulse duration as FWHM of intensity $\tau_{\text{FWHM,I}}$ [fs]	120	120
Laser peak power P_0 [TW]	997	1016
Laser oversize at interaction point n_w	1.12	3.6
Laser incident diameter D_{in} [mm]	175	175
1st grating line density n_1 [l/mm]	1000	960
1st grating incidence angle $\psi_{\text{in},1}$ [°]	40.56	26.36
1st grating incidence angle variation $\Delta\psi_{\text{in},1}$ [mrad]	14	2.8
Distance between gratings L_{grating} [mm]	3603	2828
Distance between gratings variation $\Delta L_{\text{grating}}$ [mm]	290	75
2nd grating rotation angle ϵ [°]	−4.343	−6.076
2nd grating rotation angle variation $\Delta\epsilon$ [mrad]	14	3.7
2nd grating line density n_2 [l/mm]	1030	1040
Distance between 2nd grating and off-axis cylindrical mirror L_{mirror} [mm]	2000	2000
Distance between 2nd grating and off-axis cyl. mirr. variation ΔL_{mirror} [m]	many	many
Off-axis cyl. mirror deflection angle ψ_{defl} [°]	15	15
Off-axis cyl. mirror effective focal dist. f_{eff} [mm]	32429	35854
Effective focal dist. variation Δf_{eff} [mm]	2400	1000
2nd cyl. mirror focusing dist. f_{el} [mm]	2967	4238
Out-of-focus distance Δf [mm]	-647	-8170
Propagation distance from off-axis cyl. mirror to interaction point z_{prop} [m]	31.8	27.7
Interaction angle variation $\Delta\phi$ [mrad]	14	4.6

The acceptable angle and distance variations originate solely from the variation of optical undulator amplitude due to loss of overlap, c. f. Equation (20). The undulator frequency variation is negligible within this acceptance range.

4.3. Ångström TWTS OFEL

The shorter wavelength of an Ångström TWTS OFEL allows to penetrate through thicker samples and resolve smaller structures while providing femtosecond scale temporal resolution due to its short pulse duration following from the requirement of kiloampere currents. This allows for example to determine the structure of biological specimen which can not be grown in large crystals [78] or to analyze the ultrafast dynamics of explosively driven materials at nanometer length scales [79, 80].

This example gives an outlook on the compactness of hard X-ray OFEL setups achievable with TWTS. It furthermore provides an impression on required electron and laser parameters for hard X-ray TWTS OFEL realization.

X-ray TWTS OFELs can make use of the simpler optical setup without focusing, depicted in **Figure 3**, since interaction distances and thus laser widths can be large enough to render focusing of the laser pulse unnecessary. Naturally, the electron bunch quality requirements for free-electron laser operation become stronger at shorter radiation wavelengths due to the decreased effect of radiation on the electron bunch, which is expressed by the scaling of the Pierce parameter $\rho \propto \gamma^{1/3}\lambda_{\text{FEL}}^{2/3}$ [81]. At the same time, this scaling indicates that *compact* FEL schemes, utilizing electron bunches of lower energy than conventional magnet undulator based FELs radiating at the same wavelength, additionally have increased absolute electron bunch quality requirements compared to conventional FELs.

The Ångström TWTS OFEL of this example radiates at 0.15 nm wavelength where the optical undulator with a period of 139 μm is again provided by a laser pulse of 1.035 μm wavelength and $\tau_{\text{FWHM,I}} = 120$ fs but of 576 TW peak power. It is traversed by an electron bunch at an interaction angle of 7° and an energy of about 350 MeV which is more than an order of magnitude lower than at conventional X-ray free-electrons lasers using magnetic undulators, such as LCLS [82] or SACLA [72]. Lasing is achieved with a relative electron energy spread of $\Delta\gamma/\gamma = 0.02\%$, i.e., a longitudinal emittance of 2 keV ps, and normalized transverse emittance $\epsilon_{\text{n}} = 0.2$ mm mrad at $I_{\text{p}} = 5$ kA peak current. As expected from the scaling of the Pierce parameter, the electron requirements are higher than those of conventional X-ray FELs and can not be met by present-day accelerators. For example, LCLS runs at 0.1% relative energy spread, 0.5 norm. transv. emittance and 3 kA peak current [83]. The complete parameters set of this Ångström TWTS OFEL is given in **Table 2**.

Its optical setup is depicted in **Figure 10**. The two long propagation distances, between the gratings and for focusing in the vertical direction, are set up side-by-side to save space. The long propagation distance between the gratings generates spatial dispersion which countervails spatial dispersion generated during propagation from the second grating to the interaction point. The spatial dispersion precompensation significantly increases the laser pulse width until it reaches the second grating. This grating is thus larger than the first one and has a width of 92 cm.

The choice of grating line densities is based on the requirement on laser horizontal width reduction. It needs to be decreased by almost 50% from its initial value $D_{\text{in}} = 120$ mm, which ensures a low energy density on optics, to $w_{0,yz} = 62.2$ mm which is required to achieve the target optical undulator strength over the interaction length. The relation between incident and outgoing pulse width after passing the grating pair is given by $w_{0,yz} = D_{\text{in}} \cos\psi_{\text{out},2} \cos\psi_{\text{out},1}/(\cos\psi_{\text{in},2} \cos\psi_{\text{in},1})$. A first grating line density of $n_1 = 1500$ l/mm allows for a large angular deviation between the incident and diffracted light, which is necessary to achieve the pulse width reduction of about 50%. It further provides for a large pulse-front tilt, which reduces the propagation distance between the gratings where spatial dispersion is countervailed, and permits first and second grating incidence angles to be close to their Littrow angles.

The second grating line density $n_2 = 1505$ l/mm is chosen from scalings corresponding to **Figure 8** by the requirement of

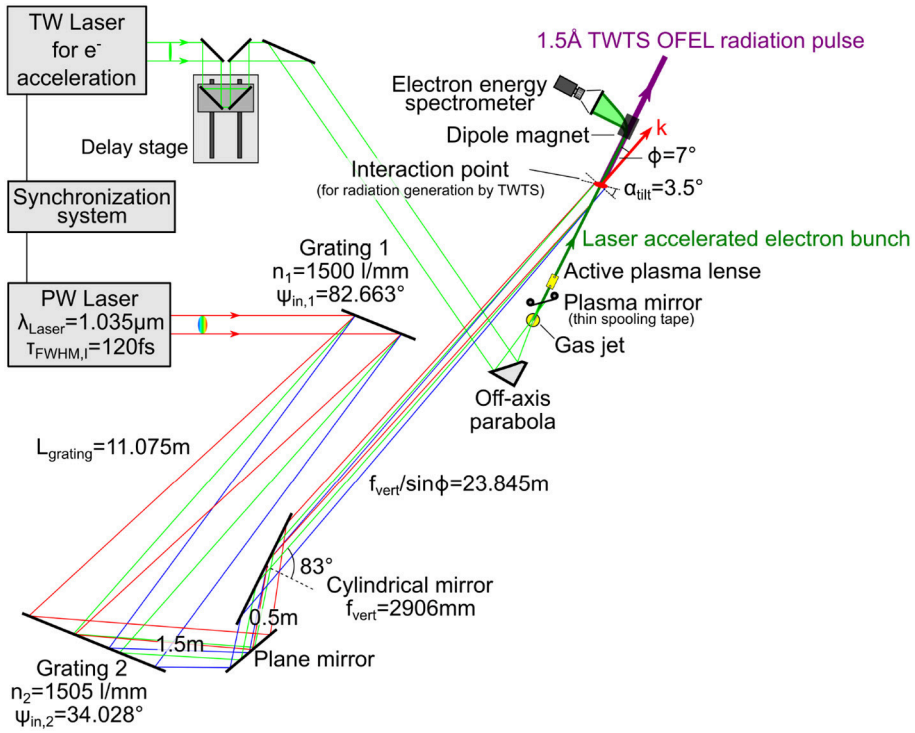

FIGURE 10 | Setup for the realization of an ultra-compact X-ray free-electron laser radiating at a wavelength of 1.5 Å. The combination of Traveling-Wave Thomson-Scattering and laser-wakefield acceleration reduces the footprint of this Ångström TWTS OFEL by orders of magnitude compared to a conventional X-ray FEL. Short laser pulses from a petawatt-class laser system are prepared in a grating setup to provide the optical undulator for TWTS. The large grating separation provides spatial dispersion precompensation which ensures vanishing spatial dispersion at the interaction point. Spatial dispersion of opposite sign develops while the tilted laser pulse covers the focusing distance f_{vert} of the vertically focusing cylindrical mirror. A terawatt-class laser system provides pulses for laser wakefield acceleration of electrons to 350 MeV. The laser systems are synchronized and a delay stage allows for fine-tuning of electron bunch and optical undulator arrival times at the interaction point.

good diffraction efficiency, i.e., allowing for a second grating incidence angle close to its Littrow angle while at the same time allowing for the correct orientation of pulse-front tilt and plane of optimum compression. Their correct orientation is ensured by the choice of first grating incidence angle $\psi_{in,1} = 82.663°$ and second grating rotation $\epsilon = -0.076°$. The complete set of optical setup parameters and their tolerances is listed in **Table 4**.

Following the discussion on alignment tolerances of the EUV TWTS OFEL, the limits set by this Ångström TWTS OFEL are achievable today as well. The second grating rotation angle ϵ is most sensitive to alignment errors this time. With variations above 30 μrad the resulting variation in pulse-front orientation becomes large enough to reduce the overlap and induce a significant intensity variation during the interaction. Thereby the longer interaction distance of the Ångström TWTS OFEL causes the increased demand on alignment accuracy compared to the EUV TWTS OFEL.

While laser systems able to provide the optical undulator exist, high brilliance electron bunches of necessary high quality have not been realized yet. However, this setup demonstrates the achievable compactness of a coherent high brightness hard X-ray source realized by a TWTS OFEL. The facility size for such a TWTS OFEL is an order of magnitude smaller compared to conventional FEL facilities due to the decreased interaction length and electron energy requirements. For a TWTS OFEL both preparation of the optical undulator and electron acceleration take place on a few ten meters, if conventional electron accelerators are used, while the interaction takes place on about a meter distance which results in an X-ray FEL facility footprint of only some hundred square meters.

5. CONCLUSION

The presented setup strategies and accompanying examples show that Traveling-Wave Thomson-Scattering (TWTS) setups can realize optical free-electron lasers (OFELs) with today available technology for electron accelerators and laser systems. The required low transverse emittance and low energy spread electron bunches can be produced by existing conventional radio-frequency electron injectors. While the operation of TWTS OFELs emitting ultraviolet radiation is feasible already, the operation of TWTS OFELs in the X-ray range requires a further increase in available electron bunch quality, e.g., by reducing the electron bunch energy spread with corrugated structures [73, 74] after acceleration.

TABLE 4 | Optical components parameters for the 1.5 Å TWTS OFEL in the setup without focusing within the interaction plane visualized in **Figure 10**.

Optical setup parameters	Å TWTS OFEL w/o focusing
Laser wavelength λ_{Laser} [μm]	1.035
Laser pulse duration as FWHM of intensity $\tau_{FWHM,I}$ [fs]	120
Laser peak power P_0 [TW]	576
Laser incident diameter D_{in} [mm]	120
1st grating line density n_1 [l/mm]	1500
1st grating incidence angle $\psi_{in,1}$ [°]	82.663
1st grating incidence angle variation $\Delta\psi_{in,1}$ [μrad]	60
Distance between gratings $L_{grating}$ [mm]	11.075×10^3
2nd grating incidence angle $\psi_{in,2}$ [°]	34.028
2nd grating rotation angle ϵ [°]	−0.076
2nd grating rotation angle variation $\Delta\epsilon$ [μrad]	29
2nd grating line density n_2 [l/mm]	1505
2nd grating diffraction angle $\psi_{out,2}$ [°]	−86.452
Distance between 2nd grating and planar mirror [mm]	1500
Planar mirror deflection angle [°]	82
Cylindrical mirror focusing dist. f_{el} [mm]	2906
Propagation distance from cyl. mirror to interaction point [m]	23.8
Interaction angle variation $\Delta\phi$ [μrad]	245

Yield-enhanced Thomson sources by TWTS radiating at a wavelength in the X- to γ-ray range are also feasible today. These could deliver radiation pulses brighter than those of any other today available source in this wavelength region. Yet they retain the compactness of high peak-brightness, all-optical Thomson sources demonstrated in the last decade since the size of both geometries is essentially determined by the size of the high-power laser system.

Regarding high peak-power laser systems, GIST [84], SIOM Qiangguang [85], BELLA [86], XL-III [87] and DRACO [88] already deliver femtosecond scale pulses of petawatt peak power [89]. Novel diode-pumped laser systems such as PENELOPE [90] and POLARIS [91] aim to offer the same power at a longer pulse duration around 100 fs which facilitates the FEL process due to reduced dispersion and better overlap with electron bunches. The alignment accuracy required in the construction of these high-power laser systems also suffices in generating TWTS pulses for TWTS OFELs, as is shown in the examples.

In the near future, even multipetawatt lasers systems such as Apollon [92], ELI [93] or SIOM OPCPA Qiangguang 10 PW [94] would allow relaxing the electron beam requirements to percent level energy spreads giving the opportunity to utilize laser wakefield accelerated (LWFA) electrons [32]. Stable production of high-quality electron beams from LWFA is an ongoing effort [95], but the necessary properties for OFEL operation were demonstrated individually already. Sub-percent level energy spreads [96], normalized transverse emittances below 1 mm mrad [97–99], as well as kiloampere currents [100, 101] through femtosecond pulse durations [102–104] and nanocoulomb-class bunch charges [105] were reported.

The combination of TWTS and high-quality LWFA, where a single high peak-power laser pulse is split and used in parts to accelerate electrons and to provide the optical undulator field, respectively, allows to operate ultra-compact, intrinsically synchronized, high peak-brilliance TWTS light sources in the ultraviolet and X-ray range. X-ray TWTS OFELs can become light sources for compact coherent X-ray scattering experiments resolving structures and processes at nanometer length and femtosecond time scales.

AUTHOR CONTRIBUTIONS

KS, DA, ML, FR, MS, and AD developed the experimental setups. KS, MB, and AD drafted the layout of the manuscript. KS wrote the first draft of the manuscript and performed calculations. RP and FR contributed to the conception, design and implementation of calculations. MB, US, and AD supervised the project. All authors contributed to manuscript revision, read and approved the submitted version.

SUPPLEMENTARY MATERIAL

The Supplementary Material for this article can be found online at: https://www.frontiersin.org/articles/10.3389/fphy.2018.00155/full#supplementary-material

REFERENCES

1. Schoenlein RW, Leemans WP, Chin AH, Volfbeyn P, Glover TE, Balling P, et al. Femtosecond X-ray Pulses at 0.4 Å Generated by 90° Thomson scattering: a tool for probing the structural dynamics of materials. *Science* (1996) **274**:236–8.
2. Pogorelsky IV, Ben-Zvi I, Hirose T, Kashiwagi S, Yakimenko V, Kusche K, et al. Demonstration of 8×10^{18}photons/second peaked at 1.8 Å in a relativistic Thomson scattering experiment. *Phys Rev ST Accel Beams.* (2000) **3**:090702. doi: 10.1103/PhysRevSTAB.3.090702
3. Pietralla N, Berant Z, Litvinenko VN, Hartman S, Mikhailov FF, Pinayev IV, et al. Parity measurements of nuclear Levels Using a Free-Electron-Laser Generated γ-Ray Beam. *Phys Rev Lett.* (2001) **88**:012502. doi: 10.1103/PhysRevLett.88.012502
4. Gibson D, Anderson S, Barty C, Betts S, Booth R, Brown W, et al. PLEIADES: a picosecond Compton scattering x-ray source for advanced backlighting and time-resolved material studies. *Phys of Plasmas.* (2004) **11**:2857–64. doi: 10.1063/1.1646160
5. Chouffani K, Harmon F, Wells D, Jones J, Lancaster G. Determination of electron beam parameters by means of laser-Compton scattering. *Phys Rev ST Accel Beams.* (2006) **9**:050701. doi: 10.1103/PhysRevSTAB.9.050701
6. Weller HR, Ahmed MW, Gao H, Tornow W, Wu YK, Gai M, et al. Research opportunities at the upgraded HIγS facility. *Progr Part Nucl Phys.* (2009) **62**:257–303. doi: 10.1016/j.ppnp.2008.07.001
7. Amano S, Horikawa K, Ishihara K, Miyamoto S, Hayakawa T, Shizuma T, et al. Several-MeV γ-ray generation at NewSUBARU by laser Compton backscattering. *Nucl Instrum Methods Phys Res A.* (2009) **602**:337–41. doi: 10.1016/j.nima.2009.01.010
8. Gibson DJ, Albert F, Anderson SG, Betts SM, Messerly MJ, Phan HH, et al. Design and operation of a tunable MeV-level Compton-scattering-based γ-ray source. *Phys Rev ST Accel Beams.* (2010) **13**:070703. doi: 10.1103/PhysRevSTAB.13.070703

9. Priebe G, Laundy D, Phillips PJ, Graham DM, Jamison SP, Vassilev S, et al. First results from the Daresbury Compton backscattering x-ray source (COBALD). In: *Proceedings SPIE Hard X-Ray, Gamma-Ray, and Neutron Detector Physics XI*. Vol. 7805 (2010). pp. 780513–14. doi: 10.1117/12.859671
10. Jochmann A, Irman A, Bussmann M, Couperus JP, Cowan TE, Debus AD, et al. High Resolution energy-angle correlation measurement of hard X rays from laser-thomson backscattering. *Phys Rev Lett.* (2013) **111**:114803. doi: 10.1103/PhysRevLett.111.114803
11. Du Y, Yan L, Hua J, Du Q, Zhang Z, Li R, et al. Generation of first hard X-ray pulse at Tsinghua Thomson Scattering X-ray Source. *Rev Sci Instrum.* (2013) **84**:053301. doi: 10.1063/1.4803671
12. Krämer JM, Jochmann A, Budde M, Bussmann M, Couperus JP, Cowan TE, et al. Making spectral shape measurements in inverse compton scattering a tool for advanced diagnostic applications. *Sci Rep.* (2018) **8**:1398. doi: 10.1038/s41598-018-19546-0
13. Faure J, Glinec Y, Pukhov A, Kiselev S, Gordienko S, Lefebvre E, et al. A laser-plasma accelerator producing monoenergetic electron beams. *Nature* (2004) **431**:541–44. doi: 10.1038/nature02963
14. Geddes CGR, Toth C, van Tilborg J, Esarey E, Schroeder CB, Bruhwiler D, et al. High-quality electron beams from a laser wakefield accelerator using plasma-channel guiding. *Nature* (2004) **431**:538–41. doi: 10.1038/nature02900
15. Mangles SPD, Murphy CD, Najmudin Z, Thomas AGR, Collier JL, Dangor AE, et al. Monoenergetic beams of relativistic electrons from intense laser-plasma interactions. *Nature* (2004) **431**:535–8. doi: 10.1038/nature02939
16. Leemans WP, Gonsalves AJ, Mao HS, Nakamura K, Benedetti C, Schroeder CB, et al. Multi-GeV electron beams from capillary-discharge-guided subpetawatt laser pulses in the self-trapping regime. *Phys Rev Lett.* (2014) **113**:245002. doi: 10.1103/PhysRevLett.113.245002
17. Esarey E, Schroeder CB, Leemans WP. Physics of laser-driven plasma-based electron accelerators. *Rev Mod Phys.* (2009) **81**:1229–85. doi: 10.1103/RevModPhys.81.1229
18. Schwoerer H, Liesfeld B, Schlenvoigt HP, Amthor KU, Sauerbrey R. Thomson-backscattered X Rays from laser-accelerated electrons. *Phys Rev Lett.* (2006) **96**:014802. doi: 10.1103/PhysRevLett.96.014802
19. Ta Phuoc K, Corde S, Thaury C, Malka V, Tafzi A, Goddet JP, et al. All-optical compton gamma-ray source. *Nature Photon.* (2012) **6**:308–11. doi: 10.1038/nphoton.2012.82
20. Mori Y, Kuwabara H, Ishii K, Hanayama R, Kawashima T, Kitagawa Y. Head-on inverse compton scattering X-rays with energy beyond 10 keV from laser-accelerated quasi-monoenergetic electron bunches. *Appl Phys Expr.* (2012) **5**:056401. doi: 10.1143/APEX.5.056401
21. Chen S, Powers ND, Ghebregziabher I, Maharjan CM, Liu C, Golovin G, et al. MeV-energy X rays from inverse compton scattering with laser-wakefield accelerated electrons. *Phys Rev Lett.* (2013) **110**:155003. doi: 10.1103/PhysRevLett.110.155003
22. Powers ND, Ghebregziabher I, Golovin G, Liu C, Chen S, Banerjee S, et al. Quasi-monoenergetic and tunable X-rays from a laser-driven Compton light source. *Nature Photon.* (2014) **8**:28–31. doi: 10.1038/nphoton.2013.314
23. Sarri G, Corvan DJ, Schumaker W, Cole JM, Di Piazza A, Ahmed H, et al. Ultrahigh brilliance multi-MeV γ-Ray beams from nonlinear relativistic thomson scattering. *Phys Rev Lett.* (2014) **113**:224801. doi: 10.1103/PhysRevLett.113.224801
24. Khrennikov K, Wenz J, Buck A, Xu J, Heigoldt M, Veisz L, et al. Tunable All-Optical Quasimonochromatic Thomson X-Ray Source in the Nonlinear Regime. *Phys Rev Lett.* (2015) **114**:195003. doi: 10.1103/PhysRevLett.114.195003
25. Döpp A, Guillaume E, Thaury C, Gautier J, Andriyash I, Lifschitz A, et al. An all-optical compton source for single-exposure x-ray imaging. *Plasma Phys Contr Fus.* (2016) **58**:034005. doi: 10.1088/0741-3335/58/3/034005
26. Yu C, Qi R, Wang W, Liu J, Li W, Wang C, et al. Ultrahigh brilliance quasi-monochromatic MeV γ-rays based on self-synchronized all-optical Compton scattering. *Sci Rep.* (2016) **6**:29518. doi: 10.1038/srep29518
27. Gea-Banacloche J, Moore G, Schlicher R, Scully M, Walther H. Soft x-ray free-electron laser with a laser undulator. *IEEE J Quant Electr.* (1987) **23**:1558–70. doi: 10.1109/JQE.1987.1073559
28. Gallardo JC, Fernow RC, Palmer R, Pellegrini C. Theory of a free-electron laser with a gaussian optical undulator. *IEEE J Quant Electr.* (1988) **24**:1557–66. doi: 10.1109/3.7085
29. Debus A, Bock S, Bussmann M, Cowan TE, Jochmann A, Kluge T, et al. Linear and non-linear thomson-scattering X-ray sources driven by conventionally and laser plasma accelerated electrons. *Proc SPIE* (2009) **7359**:735908. doi: 10.1117/12.820741
30. Debus A, Bussmann M, Siebold M, Jochmann A, Schramm U, Cowan T, et al. Traveling-wave Thomson scattering and optical undulators for high-yield EUV and X-ray sources. *Appl Phys B Las Opt.* (2010) **100**:61–76. doi: 10.1007/s00340-010-3990-1
31. Steiniger K, Bussmann M, Pausch R, Cowan T, Irman A, Jochmann A, et al. Optical free-electron lasers with Traveling-Wave Thomson-Scattering. *J Phys B.* (2014) **47**:234011. doi: 10.1088/0953-4075/47/23/234011
32. Steiniger K, Debus A, Irman A, Jochmann A, Pausch R, Schramm U, et al. Brilliant and efficient optical free-electron lasers with traveling-wave Thomson-Scattering. In: *AIP Conference Proceedings,* Vol. 1777. San Jose, CA. (2016). p. 080016. doi: 10.1063/1.4965673
33. Bacci A, Maroli C, Petrillo V, Rossi AR, Serafini L, Tomassini P. Compact X-ray free-electron laser based on an optical undulator. *Nucl Instrum Methods Phys Res A*. (2008) **587**:388–97. doi: 10.1016/j.nima.2007.12.041
34. Petrillo V, Serafini L, Tomassini P. Ultrahigh brightness electron beams by plasma-based injectors for driving all-optical free-electron lasers. *Phys Rev ST Accel Beams.* (2008) **11**:070703. doi: 10.1103/PhysRevSTAB.11.070703
35. Sprangle P, Hafizi B, Peñano JR. Laser-pumped coherent x-ray free-electron laser. *Phys Rev ST Accel Beams.* (2009) **12**:050702. doi: 10.1103/PhysRevSTAB.12.050702
36. Lawler JE, Bisognano J, Bosch RA, Chiang TC, Green MA, Jacobs K, et al. Nearly copropagating sheared laser pulse FEL undulator for soft x-rays. *J Phys D* (2013) **46**:325501. doi: 10.1088/0022-3727/46/32/325501
37. Chang C, Liang J, Hei D, Becker MF, Tang K, Feng Y, et al. High-brightness X-ray free-electron laser with an optical undulator by pulse shaping. *Opt Express.* (2013) **21**:32013–18. doi: 10.1364/OE.21.032013
38. Andriyash I, Balcou P, Tikhonchuk V. Collective properties of a relativistic electron beam injected into a high intensity optical lattice. *Eur Phys J D.* (2011) **65**:533–40. doi: 10.1140/epjd/e2011-20254-5
39. Andriyash IA, d'Humières E, Tikhonchuk VT, Balcou P. X-Ray Amplification from a Raman Free-Electron Laser. *Phys Rev Lett.* (2012) **109**:244802. doi: 10.1103/PhysRevLett.109.244802
40. Chang C, Tang C, Wu J. High-gain thompson-scattering X-ray free-electron laser by time-synchronic laterally tilted optical wave. *Phys Rev Lett.* (2013) **110**:064802. doi: 10.1103/PhysRevLett.110.064802
41. Ride SK, Esarey E, Baine M. Nonlinear Thomson scattering of intense lasers from electron beams at arbitrary interaction angles. *Phys Rev E.* (1995) **52**:5425–42. doi: 10.1103/PhysRevE.48.3003
42. Martinez OE. Pulse distortions in tilted pulse schemes for ultrashort pulses. *Opt Commun.* (1986) **59**:229–32. doi: 10.1016/0030-4018(86)90290-7
43. Akturk S, Gu X, Zeek E, Trebino R. Pulse-front tilt caused by spatial and temporal chirp. *Opt Express.* (2004) **12**:4399–410. doi: 10.1364/OPEX.12.004399
44. Chanteloup JC, Salmon E, Sauteret C, Migus A, Zeitoun P, Klisnick A, et al. Pulse-front control of 15-TW pulses with a tilted compressor, and application to the subpicosecond traveling-wave pumping of a soft-x-ray laser. *J Opt Soc Am B.* (2000) **17**:151–7. doi: 10.1364/JOSAB.17.000151
45. Huang Z, Kim KJ. Review of x-ray free-electron laser theory. *Phys Rev ST Accel Beams.* (2007) **10**:034801. doi: 10.1103/PhysRevSTAB.10.034801
46. Bonifacio R, Pellegrini C, Narducci L. Collective instabilities and high-gain regime in a free electron laser. *Opt Commun.* (1984) **50**:373–8. doi: 10.1016/0030-4018(84)90105-6
47. Kim KJ. An analysis of self-amplified spontaneous emission. *Nucl Instrum Methods Phys Res A.* (1986) **250**:396–403. doi: 10.1016/0168-9002(86)90916-2
48. Schmüser P, Dohlus M, Rossbach J, Behrens C. *Free-Electron Laser in the Ultraviolet and X-Ray Regime.* Springer Tracts in Modern Physics 258. Springer International Publishing Switzerland (2014). doi: 10.1007/978-3-319-04081-3
49. Spectrogon AB. *Grating Glossary*. Available online at: http://www.spectrogon.com/product-services/gratings/glossary

50. Zhu G, van Howe J, Durst M, Zipfel W, Xu C. Simultaneous spatial and temporal focusing of femtosecond pulses. *Opt Express.* (2005) **13**:2153–9. doi: 10.1364/OPEX.13.002153
51. Siegmann A. *Lasers*. University Science Books (1986).
52. Zemax LLC. *Zemax - Optical Design Software* (2016). Available online at: www.zemax.com
53. Schulz S, Grguraš I, Behrens C, Bromberger H, Costello J, Czwalinna M, et al. Femtosecond all-optical synchronization of an X-ray free-electron laser. *Nat Commun.* (2015) **6**:5938. doi: 10.1038/ncomms6938
54. Wabnitz H, Bittner L, De Castro A, Döhrmann R, Gürtler P, Laarmann T, et al. Multiple ionization of atom clusters by intense soft X-rays from a free-electron laser. *Nature* (2002) **420**:482–5. doi: 10.1038/nature01197
55. Pfeifer T, Spielmann C, Gerber G. Femtosecond x-ray science. *Reports Progr Phys.* (2006) **69**:443. doi: 10.1088/0034-4885/69/2/R04
56. Pietzsch A, Föhlisch A, Beye M, Deppe M, Hennies F, Nagasono M, et al. Towards time resolved core level photoelectron spectroscopy with femtosecond x-ray free-electron lasers. *N J Phys.* (2008) **10**:033004. doi: 10.1088/1367-2630/10/3/033004
57. Krzywinski J, Sobierajski R, Jurek M, Nietubyc R, Pelka JB, Juha L, et al. Conductors, semiconductors, and insulators irradiated with short-wavelength free-electron laser. *J Appl Phys.* (2007) **101**:043107. doi: 10.1063/1.2434989
58. Barke I, Hartmann H, Rupp D, Flückiger L, Sauppe M, Adolph M, et al. The 3D-architecture of individual free silver nanoparticles captured by X-ray scattering. *Nat Commun.* (2015) **6**:187. doi: 10.1038/ncomms7187
59. Barty A, Boutet S, Bogan MJ, Hau-Riege S, Marchesini S, Sokolowski-Tinten K, et al. Ultrafast single-shot diffraction imaging of nanoscale dynamics. *Nature Photon.* (2008) **2**:415–9. doi: 10.1038/nphoton.2008.128
60. Mazza T, Karamatskou A, Ilchen M, Bakhtiarzadeh S, Rafipoor A, OKeeffe P, et al. Sensitivity of nonlinear photoionization to resonance substructure in collective excitation. *Nat Commun.* (2015) **6**:6799. doi: 10.1038/ncomms7799
61. Gaudin J, Medvedev N, Chalupský J, Burian T, Dastjani-Farahani S, Hájková V, et al. Photon energy dependence of graphitization threshold for diamond irradiated with an intense XUV FEL pulse. *Phys Rev B.* (2013) **88**:060101. doi: 10.1103/PhysRevB.88.060101
62. Wagner C, Harned N. EUV lithography: lithography gets extreme. *Nature Photon.* (2010) **4**:24–6. doi: 10.1038/nphoton.2009.251
63. Ackermann W, Asova G, Ayvazyan V, Azima A, Baboi N, Bähr J, et al. Operation of a free-electron laser from the extreme ultraviolet to the water window. *Nature Photonics.* (2007) **1**:336–42. doi: 10.1038/nphoton.2007.76
64. Allaria E, Castronovo D, Cinquegrana P, Craievich P, Dal Forno M, Danailov M, et al. Two-stage seeded soft-X-ray free-electron laser. *Nature Photon.* (2013) **7**:913–8. doi: 10.1038/nphoton.2013.277
65. Togawa K, Shintake T, Inagaki T, Onoe K, Tanaka T, Baba H, et al. CeB_6 electron gun for low-emittance injector. *Phys Rev ST Accel Beams.* (2007) **10**:020703. doi: 10.1103/PhysRevSTAB.10.020703
66. Ding Y, Brachmann A, Decker FJ, Dowell D, Emma P, Frisch J, et al. Measurements and simulations of ultralow emittance and ultrashort electron beams in the Linac Coherent Light Source. *Phys Rev Lett.* (2009) **102**:254801. doi: 10.1103/PhysRevLett.102.254801
67. Arnold A, Teichert J. Overview on superconducting photoinjectors. *Phys Rev ST Accel Beams.* (2011) **14**:024801. doi: 10.1103/PhysRevSTAB.14.024801
68. Krasilnikov M, Stephan F, Asova G, Grabosch HJ, Groß M, Hakobyan L, et al. Experimentally minimized beam emittance from an *L*-band photoinjector. *Phys Rev ST Accel Beams.* (2012) **15**:100701. doi: 10.1103/PhysRevSTAB.15.100701
69. Gulliford C, Bartnik A, Bazarov I, Cultrera L, Dobbins J, Dunham B, et al. Demonstration of low emittance in the Cornell energy recovery linac injector prototype. *Phys Rev ST Accel Beams.* (2013) **16**:073401. doi: 10.1103/PhysRevSTAB.16.073401
70. Penco G, Allaria E, Badano L, Cinquegrana P, Craievich P, Danailov M, et al. Optimization of a high brightness photoinjector for a seeded FEL facility. *J Instrument.* (2013) **8**:P05015. doi: 10.1088/1748-0221/8/05/P05015
71. Prat E, Aiba M, Bettoni S, Beutner B, Reiche S, Schietinger T. Emittance measurements and minimization at the SwissFEL injector test facility. *Phys Rev ST Accel Beams.* (2014) **17**:104401. doi: 10.1103/PhysRevSTAB.17.104401
72. Ishikawa T, Aoyagi H, Asaka T, Asano Y, Azumi N, Bizen T, et al. A compact X-ray free-electron laser emitting in the sub-angstrom region. *Nature Photon.* (2012) **6**:540–4. doi: 10.1038/nphoton.2012.141
73. Deng H, Zhang M, Feng C, Zhang T, Wang X, Lan T, et al. Experimental demonstration of longitudinal beam phase-space linearizer in a free-electron laser facility by corrugated structures. *Phys Rev Lett.* (2014) **113**:254802. doi: 10.1103/PhysRevLett.113.254802
74. Fu F, Wang R, Zhu P, Zhao L, Jiang T, Lu C, et al. Demonstration of nonlinear-energy-spread compensation in relativistic electron bunches with corrugated structures. *Phys Rev Lett.* (2015) **114**:114801. doi: 10.1103/PhysRevLett.114.114801
75. Hornung M, Bödefeld R, Siebold M, Schnepp M, Hein J, Sauerbrey R, et al. Alignment of a tiled-grating compressor in a high-power chirped-pulse amplification laser system. *Appl opt.* (2007) **46**:7432–5. doi: 10.1364/AO.46.007432
76. Zeil K, Metzkes J, Kluge T, Bussmann M, Cowan TE, Kraft SD, et al. Direct observation of prompt pre-thermal laser ion sheath acceleration. *Nat Commun.* (2012) **3**:874. doi: 10.1038/ncomms1883
77. Yakovlev IV. Stretchers and compressors for ultra-high power laser systems. *Quan Electr.* (2014) **44**:393. doi: 10.1070/QE2014v044n05ABEH015429
78. Boutet S, Lomb L, Williams GJ, Barends TRM, Aquila A, Doak RB, et al. High-resolution protein structure determination by serial femtosecond crystallography. *Science* (2012) **337**:362–4. doi: 10.1126/science.1217737
79. Kraus D, Ravasio A, Gauthier M, Gericke D, Vorberger J, Frydrych S, et al. Nanosecond formation of diamond and lonsdaleite by shock compression of graphite. *Nat Commun.* (2016) **7**:10970. doi: 10.1038/ncomms10970
80. Kluge T, Bussmann M, Chung HK, Gutt C, Huang LG, Zacharias M, et al. Nanoscale femtosecond imaging of transient hot solid density plasmas with elemental and charge state sensitivity using resonant coherent diffraction. *Phys Plasmas.* (2016) **23**:33103. doi: 10.1063/1.4942786
81. Steiniger K, Debus A, Irman A, Jochmann A, Pausch R, Schramm U, et al. All-optical free-electron lasers using Traveling-Wave Thomson-Scattering. In: *IPAC2014 - Proceedings.* Dresden. (2014). doi: 10.18429/JACoW-IPAC2014-WEPRO053
82. Emma P, Akre R, Arthur J, Bionta R, Bostedt C, Bozek J, et al. First lasing and operation of an ångstrom-wavelength free-electron laser. *Nature Photonics.* (2010) **4**:641–7. doi: 10.1038/nphoton.2010.176
83. LCLS Parameters–March 2017;. *Machine Parameters Table.* Available online at: https://portal.slac.stanford.edu/sites/lcls_public/Lists/machine_faq/FAQ.aspx
84. Sung JH, Lee SK, Yu TJ, Jeong TM, Lee J. 0.1 Hz 1.0 PW Ti: sapphire laser. *Opt Lett.* (2010) **35**:3021–3. doi: 10.1364/OL.35.003021
85. Chu Y, Liang X, Yu L, Xu Y, Xu L, Ma L, et al. High-contrast 2.0 Petawatt Ti: sapphire laser system. *Opt Expr.* (2013) **21**:29231–9. doi: 10.1364/OE.21.029231
86. Nakamura K, Mao H, Gonsalves AJ, Vincenti H, Mittelberger DE, Daniels J, et al. Diagnostics, Control and Performance Parameters for the BELLA High Repetition Rate Petawatt Class Laser. *IEEE J Quan Electr.* (2017) **53**:1–21. doi: 10.1109/JQE.2017.2708601
87. Wang Z, Liu C, Shen Z, Zhang Q, Teng H, Wei Z. High-contrast 1.16 PW Ti: sapphire laser system combined with a doubled chirped-pulse amplification scheme and a femtosecond optical-parametric amplifier. *Opt Lett.* (2011) **36**:3194–6. doi: 10.1364/OL.36.003194
88. Schramm U, et al. First results with the novel Peta-Watt Laser Acceleration Facility in Dresden. In: *Proceedings of International Particle Accelerator Conference (IPAC'17)*, 14-19 May, 2017. No. 8 *in International Particle Accelerator Conference.* Copenhagenl; Geneva: JACoW (2017). pp. 48–52. Available online at : http://jacow.org/ipac2017/papers/mozb1.pdf
89. Danson C, Hillier D, Hopps N, Neely D. Petawatt class lasers worldwide. *High Power Laser Sci Eng.* (2015) **3**:e3. doi: 10.1017/hpl.2014.52
90. Siebold M, Roeser F, Loeser M, Albach D, Schramm U. PEnELOPE - a high peak-power diode-pumped laser system for laser-plasma experiments. *Proc SPIE.* (2013) n**8780**:878005. doi: 10.1117/12.2017522
91. Hornung M, Keppler S, Bödefeld R, Kessler A, Liebetrau H, Körner J, et al. High-intensity, high-contrast laser pulses generated from the fully

diode-pumped Yb: glass laser system POLARIS. *Opt Lett.* (2013) **38**:718–20. doi: 10.1364/OL.38.000718
92. Zou J, Le Blanc C, Papadopoulos D, Chériaux G, Georges P, Mennerat G, et al. Design and current progress of the Apollon 10 PW project. *High Power Laser Sci Eng.* (2015) **3**:e2. doi: 10.1017/hpl.2014.41
93. Extreme Light. *Nat Mater*. (2016) **15**:1. doi: 10.1038/nmat4533
94. Xu L, Yu L, Liang X, Chu Y, Hu Z, Ma L, et al. High-energy noncollinear optical parametric-chirped pulse amplification in LBO at 800nm. *Opt Lett*. (2013) **38**:4837–40. doi: 10.1364/OL.38.004837
95. Downer MC, Zgadzaj R, Debus A, Schramm U, Kaluza MC. Diagnostics for plasma-based electron accelerators. *Rev Mod Phys.* (2018) **90**:035002. doi: 10.1103/RevModPhys.90.035002
96. Wang WT, Li WT, Liu JS, Zhang ZJ, Qi R, Yu CH, et al. High-brightness high-energy electron beams from a laser wakefield accelerator via energy chirp Control. *Phys Rev Lett.* (2016) **117**:124801. doi: 10.1103/PhysRevLett.117.124801
97. Kneip S, McGuffey C, Martins JL, Bloom MS, Chvykov V, Dollar F, et al. Characterization of transverse beam emittance of electrons from a laser-plasma wakefield accelerator in the bubble regime using betatron x-ray radiation *Phys Rev ST Accel Beams.* (2012) **15**:021302. doi: 10.1103/PhysRevSTAB.15.021302
98. Weingartner R, Raith S, Popp A, Chou S, Wenz J, Khrennikov K, et al. Ultralow emittance electron beams from a laser-wakefield accelerator. *Phys Rev ST Accel Beams.* (2012) **15**:111302. doi: 10.1103/PhysRevSTAB.15.111302
99. Plateau GR, Geddes CGR, Thorn DB, Chen M, Benedetti C, Esarey E, et al. Low-emittance electron bunches from a laser-plasma accelerator measured using single-shot X-Ray spectroscopy. *Phys Rev Lett.* (2012) **109**:064802. doi: 10.1103/PhysRevLett.109.064802
100. Lundh O, Lim J, Rechatin C, Ammoura L, Ben-Ismail A, Davoine X, et al. Few femtosecond, few kiloampere electron bunch produced by a laser-plasma accelerator. *Nat Phys*. (2011) **7**:219–22. doi: 10.1038/nphys1872
101. Li YF, Li DZ, Huang K, Tao MZ, Li MH, Zhao JR, et al. Generation of 20 kA electron beam from a laser wakefield accelerator. *Phys Plasmas.* (2017) **24**:023108. doi: 10.1063/1.4975613
102. van Tilborg J, Schroeder CB, Filip CV, Tóth C, Geddes CGR, Fubiani G, et al. Temporal characterization of femtosecond laser-plasma-accelerated electron bunches using terahertz radiation. *Phys Rev Lett.* (2006) **96**:014801. doi: 10.1103/PhysRevLett.96.014801
103. Debus AD, Bussmann M, Schramm U, Sauerbrey R, Murphy CD, Major Z, et al. Electron bunch length measurements from laser-accelerated electrons using single-shot THz time-domain interferometry. *Phys Rev Lett.* (2010) **104**:084802. doi: 10.1103/PhysRevLett.104.084802
104. Buck A, Nicolai M, Schmid K, Sears CMS, Savert A, Mikhailova JM, et al. Real-time observation of laser-driven electron acceleration. *Nature Phys.* (2011) **7**:543–8. doi: 10.1038/nphys1942
105. Couperus J, Pausch R, Köhler A, Zarini O, Krämer J, Garten M, et al. Demonstration of a beam loaded nanocoulomb-class laser wakefield accelerator. *Nat Commun.* (2017) **8**:487. Available online at: doi: 10.1038/s41467-017-00592-7
106. Steiniger K, Widera R, Pausch R, Debus A, Bussmann M, Schramm U. Wave optical description of the Traveling-Wave Thomson-Scattering optical undulator field and its application to the TWTS-FEL . *Nucl Instrum Methods Phys Res A.* (2014) **740**:147–52. doi: 10.1016/j.nima.2013.10.091
107. O'Shea DC. Group velocity dispersion using commercial optical design programs. *Appl Opt.* (2006) **45**:4740–6. doi: 10.1364/AO.45.004740

Conflict of Interest Statement: The authors declare that the research was conducted in the absence of any commercial or financial relationships that could be construed as a potential conflict of interest.